Geol. Mag. **147** (*3*), *2010, pp. 434–450. © Cambridge University Press 2009*
doi:10.1017/S0016756809990550

High-Mg potassic rocks in the Balkan segment of the Variscan belt (Bulgaria): implications for the genesis of orogenic lamproite magmas

L. BUZZI*, L. GAGGERO*†, L. GROZDANOV‡, S. YANEV‡ & F. SLEJKO§

*Department for the Study of Territory and its Resources, University of Genoa, Corso Europa 26, I-16132 Genoa, Italy
‡Geological Institute of the Bulgarian Academy of Sciences, G. Bonchev Str. Bl. 24, 1113 Sofia, Bulgaria
§Department of Earth Sciences, University of Trieste, Via Weiss 8, I-34127 Trieste, Italy

(*Received* 6 May 2009; *accepted* 11 August 2009; First published online 27 October 2009)

Abstract – Ultrapotassic plutons from several domains of the Variscan orogenic belt have been in turn interpreted as syn- to post-orogenic due to their age spread, but assessment of their geodynamic setting and source regions is still open to interpretation. In the Svoge region (Bulgaria), at the southern margin of the Balkan orogen, peralkalic plutons are hosted within Ordovician pelites. The main intrusion, with lamproitic affinity, which hosts monzodiorite xenoliths and a polyphase syenite suite, was emplaced at a shallow level. ^{40}Ar–^{39}Ar dating by step-heating of amphibole and biotite yielded a Early Carboniferous intrusion age for the main body (337 ± 4 and 339.1 ± 1.6 Ma). The lamproite intrusion is silica-rich compared with bona fide lamproites and characterized by moderate LILE and La_N/Yb_N enrichments. Sr and Nd isotopic data (initial ε_{Nd} in the range -4.87 to -5.88) suggest an origin in a depleted lithospheric mantle, possibly refertilized by eo-Variscan subduction. The high-K syn-tectonic plutonism in several zones of the Variscan orogen (Bohemian, Austro-Alpine, Vosges, French and Corsica domains) is consistent with a derivation of high-K magmatism from partial melting of metasomatized mantle following the subduction along the collision front between Gondwana and Laurasia.

Keywords: ultrapotassic, ^{39}Ar–^{40}Ar dating, Sr–Nd, Balkan terrane, Early Carboniferous, syn-orogenic.

1. Introduction

The Balkan orogen includes several pre-Ordovician microcontinents, which originated on the margins of Gondwana and which accreted during the Variscan event (Haydoutov & Yanev, 1997; Yanev, 2000; von Raumer, Stampfli & Bussy, 2003 and references therein). In the eastern part of the Balkan peninsula, several structural units of peri-Gondwanan origin have been identified (Fig. 1a): (1) the Moesian terrane, (2) the Balkan terrane (Haydoutov & Yanev, 1997) and (3) the Thracian composite superterrane (Haydoutov *et al.* 2004), including the terranes of Sredna Gora, Rila, Rhodope, Pirin, Ograzhden and the Osogovo mountains. After the Devonian convergence of the Moesian terrane and Dobrudgea, the peri-Gondwanan Moesian terrane and the Balkan and Thracian blocks collided, and then docked to Palaeo-Europe during Carboniferous times (Yanev, 2000).

Coeval ultrapotassic plutons (Table 1) related to post-Variscan collision (Bonin, 2004) are known from several branches of the Variscan orogen, including southern Hungary (Buda & Dobosi, 2004; Klötzli, Buda & Skiöld, 2004), the Bohemian Massif (Holub, Cocherie & Rossi, 1997; Wenzel *et al.* 1997; Nasdala *et al.* 1999; Gerdes, Wöerner & Finger, 2000; Janousek & Holub, 2007), the eastern Tauern Window (Finger *et al.* 1997), the Vosges (Langer *et al.* 1995; Schaltegger *et al.* 1996), the External Crystalline Massifs of the Alps (Aar Massif: Schaltegger *et al.* 1991; Belledonne Massifs: Debon *et al.* 1998; von Raumer, Bussy & Stampfli, 2009), the French Massif Central (Livradois area: Solgadi *et al.* 2007) and Corsica (Cocherie *et al.* 1994; Paquette *et al.* 2003). These plutons were emplaced syntectonically along major dextral strike-slip faults (von Raumer, Bussy & Stampfli, 2009). The lateral extent of Carboniferous magmatism points to the development along a major alignment, which up to now has mostly been investigated in the central and southern Variscides. However, in the southeastern European domains, the ages of similar suites are quite different (Vladykin, Grozdanov & Bonev, 2001) and their source region remains largely speculative.

We have investigated peralkalic plutons intruded in Ordovician country rocks from the Svoge region, at the southern margin of the Balkan orogenic belt. The ^{40}Ar–^{39}Ar radiometric age, the elemental and the Sr–Nd isotopic fingerprints of this ultrapotassic magmatism help identify the igneous sources, characterizing this step of the Variscan history in the southeastern Balkan sector, and drawing possible correlations within the regional geodynamics.

2. Geological setting

The basement of the Balkan terrane comprises a Neoproterozoic ophiolite and a Cambro-Ordovician

†Author for correspondence: gaggero@dipteris.unige.it

Table 1. Geochronological data from Variscan magnesio-potassic plutons from central and eastern Europe

Occurrence	Lithology	Age	Dating technique	References
Mórágy Hills (southern Hungary)	Quartz monzonite and monzogranite	339 ± 10 Ma	Single-zircon ^{207}Pb–^{206}Pb evaporation	Klötzli, Buda & Skiöld, 2004
Central Bohemian Plutonic Complex	Melagranite	343 ± 6 Ma; 340 ± 8 Ma	Single-zircon ^{207}Pb–^{206}Pb evaporation	Holub, Cocherie & Rossi, 1997
Meissen Massif (Germany)	Monzonite	330 ± 5 Ma; 326 ± 6 Ma 330.4 ± 1.4 Ma; 329.1 ± 1.4 Ma	SHRIMP U–Pb on zircon ^{40}Ar–^{39}Ar on amphibole	Nasdala *et al.* 1999 Wenzel *et al.* 1997
Vosges (France)	Granite	340 ± 1 Ma	U–Pb dissolution	Schaltegger *et al*. 1996
Belledonne Massif (western Alps)	Biotite granites and granodiorites	343 ± 16 Ma; 341 ± 13 Ma; 335 ± 13 Ma;	Single-zircon ^{207}Pb–^{206}Pb evaporation	Debon *et al*. 1998
Corsica	Monzonite to leucosyenogranite	337 ± 2 Ma	ID-TIMS U–Pb on zircon	Paquette *et al*. 2003
		322 ± 12 Ma	Single-zircon ^{207}Pb–^{206}Pb evaporation	Cocherie, Guerrot & Rossi, 1992

island arc association (Haydoutov, 1989; Savov *et al.* 2001), unconformably overlain by a Palaeozoic sedimentary sequence, which is intruded by a post-Variscan calc-alkalic volcanic suite (Cortesogno *et al.* 2004).

On the southern margin of the Balkan terrane (Svoge region), mafic plutons have intruded at a relatively shallow depth (andalusite + biotite in the contact aureole) within the Middle–Upper Ordovician grey shales and sandstones of the Grohoten Formation (Vladykin, Grozdanov & Bonev, 2001; Gutiérrez-Marco *et al.* 2003).

Polyphase plugs and dykes of syenite composition cut the plutons. A mafic pluton and related syenitic to quartz syenitic intrusions extending for about 2.5 km^2 have been studied in detail for the Svidnya river valley (Fig. 1b).

3. Petrography

3.a. The mafic pluton

The Svidnya main intrusion, described as shonkinite or lamproite in the regional literature (Grozdanov, 1965; Stefanova, 1966; Vladykin, Grozdanov & Bonev, 2001), shows essentially two compositions: (1) diopside–sanidine–phlogopite lamproite (formerly orendite) according to the IUGS nomenclature (Woolley *et al.* 1996), characterized by lack of primary plagioclase, and (2) aegirine, Na–Ca and Na-amphibole, potassic and sodic feldspar melasyenite.

As a rule, both compositions show medium- to coarse-grained (1–10 mm) phaneritic texture and fine- to medium-grained (0.5–1 mm) porphyritic texture. Flow textures can develop, but generally the large K-feldspar phenocrysts do not exhibit a preferred orientation. Locally, the early-crystallized mafic phases develop cumulus features (Figs 2, 3a; a colour version of Fig. 3 is available in online Appendix at http://www.cambridge.org/journals/geo).

The lamproite is characterized by early-crystallized Fe-rich K-feldspar, diopsidic augite and high-Ti biotite (Fig. 3b). K-feldspar exhibits growth zoning and synneusis from a light-coloured core. Diopsidic

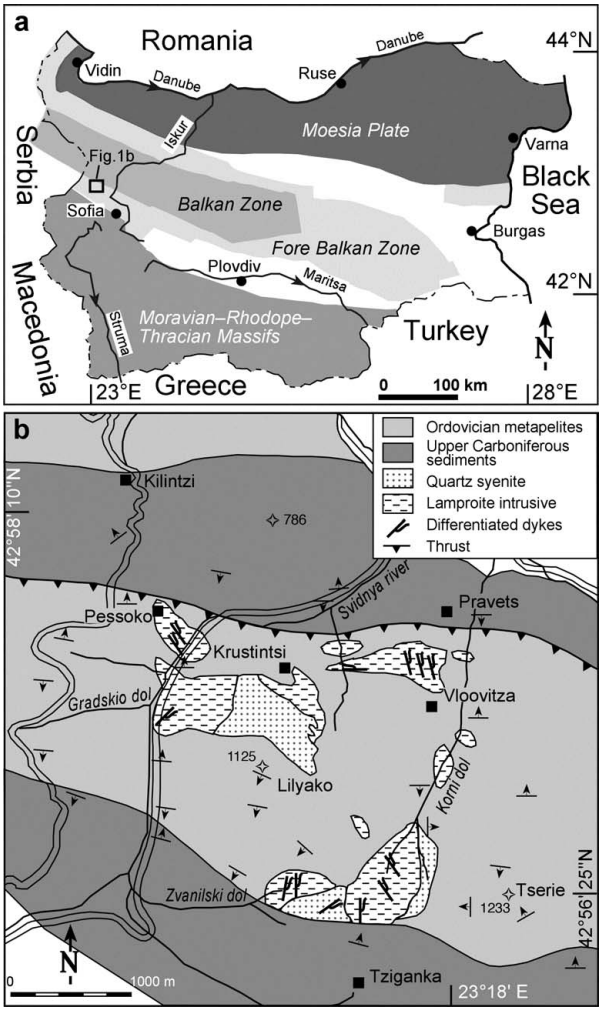

Figure 1. (a) Sketch map of the main Variscan structures in Bulgaria. Blank areas represent the alluvial cover. (b) Geological map of the Svidnya basin.

augites occasionally show overgrowths of, or partial replacement by, richterite, winchite and actinolite. Biotite, frequently including pyroxene and apatite, is intergrown with and mantled by subhedral richterite (Fig. 3c). Sometimes biotite shows deformed reddish cores and undeformed orange-reddish rims with oxide inclusions. A few lamproites, lacking diopsidic augite,

https://doi.org/10.1017/S0016756809990550 Published online by Cambridge University Press

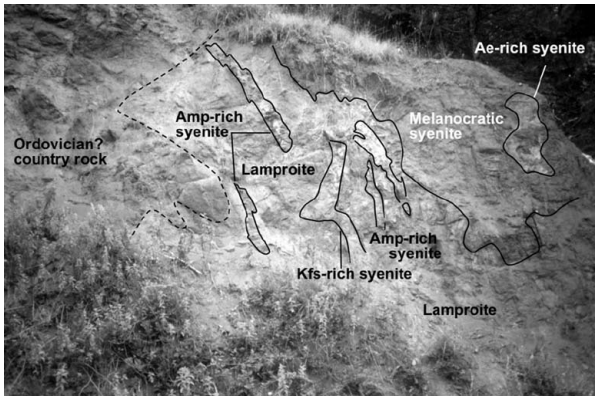

Figure 2. Intrusion relationships of lamproites, syenites and country rock at Svidnya. The present setting of contact surfaces is at high, nearly vertical dip. The field of view is about 5.85 m wide. A colour version of this figure is available at http://www.cambridge.org/journals/geo.

are instead characterized by amphibole and biotite pseudomorphs after olivine (Fig. 3d). Biotite coronas around these pseudomorphs suggest that decompression occurred during cooling. Very fine-grained mosaic biotite and K-feldspar crystallize in rounded aggregates up to 0.5 cm in olivine-bearing lamproites. Dark brown biotites, rimmed by reddish biotite, develop inside the patches (Fig. 4b, Table 3). Within amphibole and biotite, early-crystallized apatite, with pinkish cores and evident growth zoning, is abundant, and late-precipitated apatite is generally colourless. Zircon, titanite, Fe-oxides and scarce galena are accessory phases. The amphibole core is occasionally altered to calcite or, more rarely, barite and Th-, LREE-phosphates.

Melasyenites are found in the main intrusion and also as thin porphyritic dykes. In melasyenites, the abundant albite exhibits silicate and clouds of oxide microinclusions, whereas the potassic feldspar shows perthite exsolutions. Clinopyroxenes are zoned with aegirine–augite cores grading to aegirine rims. Na–Ca and finally Na-amphiboles crystallize cotectically with K-feldspar and aegirine. In turn, poikilitic biotite with included crystals of K-feldspar and richterite is partly intergrown with Na-amphibole. Amphibole also occurs as radiating clusters, characterized by needle-shaped ferri-eckermannite at the core, likely replacing

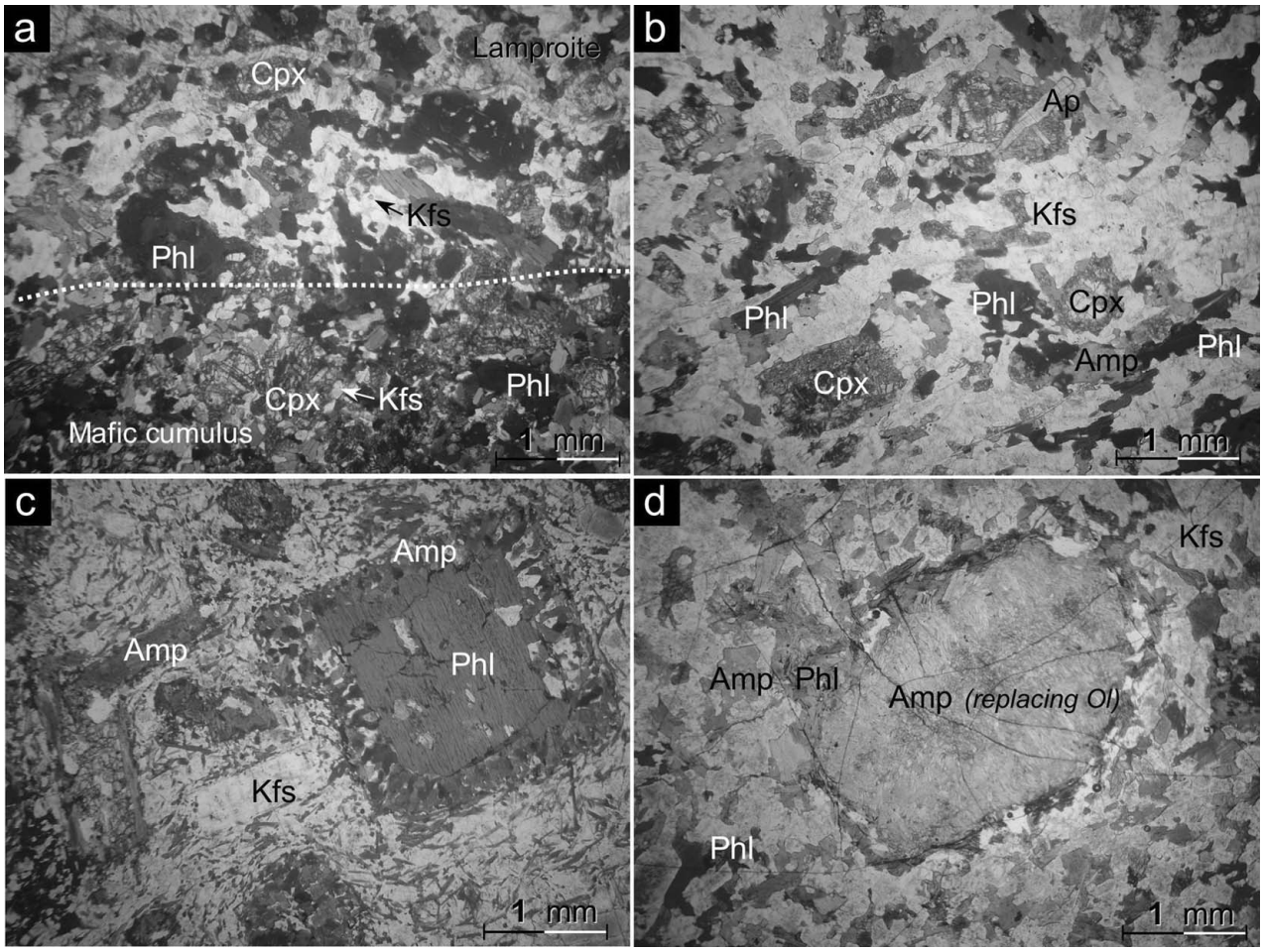

Figure 3. Microphotographs of Svidnya lamproites. Plane polarized light. Scale bar in the photographs. (a) Cumulus texture of clinopyroxene and biotite with K-feldspar as intercumulus phase. (b) Phaneritic medium-grained texture of clinopyroxene, biotite and K-feldspar. (c) Subhedral biotite, poikilitic on apatite and pyroxene, mantled by green amphibole aggregates. (d) Biotite coronas surrounding amphibole pseudomorphs after olivine. For a colour version of this figure see online Appendix at http://journals.cambridge.org/geo.

https://doi.org/10.1017/S0016756809990550 Published online by Cambridge University Press

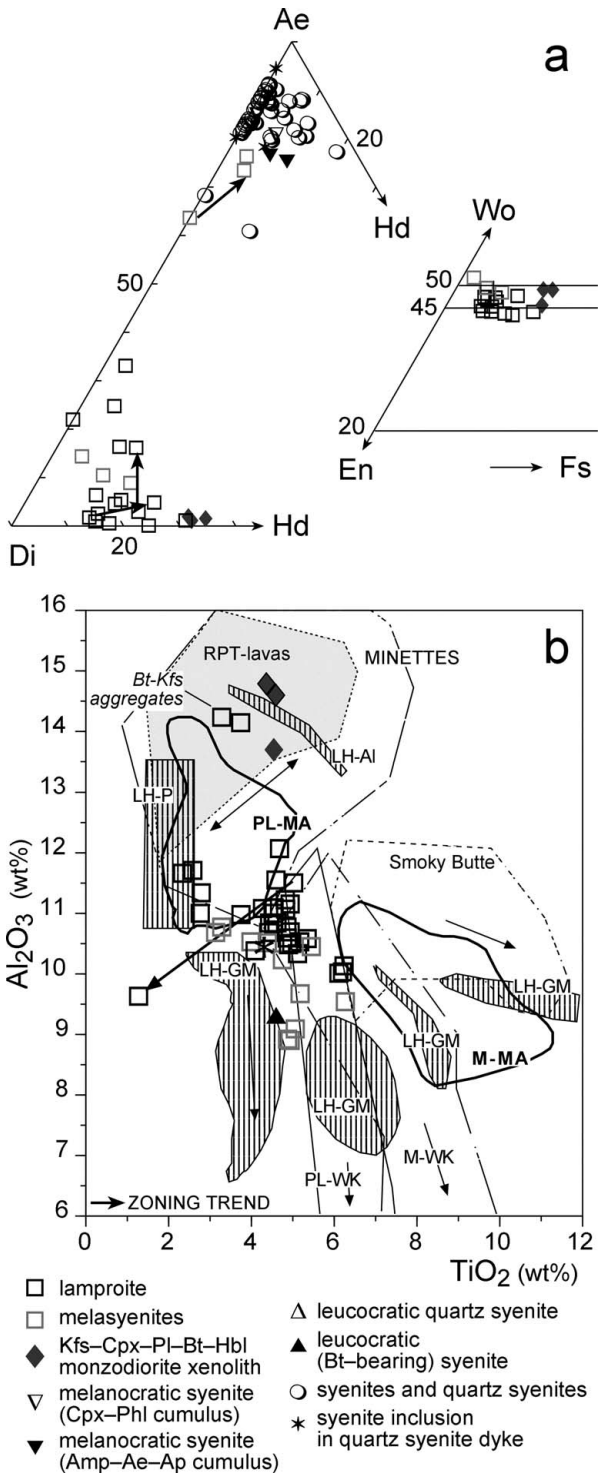

Figure 4. (a) Ae ($NaFe^{3+}Si_2O_6$) – Di ($CaMgSi_2O_6$) – Hd ($CaFe^{2+}Si_2O_6$) and Wo–En–Fs diagram for clinopyroxenes from lamproites and syenites. (b) Al_2O_3 v. TiO_2 diagram for phlogopites. For comparison in (b), compositional fields of brown-micas from minettes, Roman Province lavas (RPT-lavas) and lamproites are reported. Data from Mitchell & Bergman (1991). Abbreviations: LH-Al – aluminous phlogopite in inclusions from Leucite Hills; LH-GM – groundmass/madupitic micas from Leucite Hills; LH-P – phenocrysts from Leucite Hills; M-MA – madupitic lamproite Murcia Almeria; M-WK – madupitic lamproite West Kimberley; PL-MA – phlogopite lamproite Murcia Almeria; PL-WK – phlogopite lamproite West Kimberley.

biotite or clinopyroxene, and secondary fibrous green richterite at the rim. Accessory phases are zircon, titanite, apatite and rare Ba- and Nb-titanosilicates.

3.b. Plugs and dykes

Syenites and quartz syenites are medium-coarse (1–6 mm), with heterogranular, hypidiomorphic granular to porphyritic textures (Fig. 5a, b). They range from melanocratic to leucocratic, due to cumulus processes (e.g. Fig. 5b–d), and from primitive to evolved compositions. The more primitive compositions are characterized by early cotectic crystallization of K-feldspar + Na–Ca amphibole, followed by the K-feldspar + Na-amphibole + aegirine assemblage in intermediate compositions, and finally by K-feldspar + aegirine in more evolved ones. Prismatic K-feldspar frequently forms radiating sprays, or includes apatite and aegirine. Quartz is a common interstitial phase.

Melanocratic syenites are characterized by orthocumulus textures (Fig. 5c, d). The cumulus phases are dominantly zoned richterite (up to 80 % in volume), overgrown along cleavages or partially replaced by eckermannite and ferri-glaucofane. Na-clinopyroxene, K-feldspar and apatite precipitate as cumulus phases, K-feldspar and quartz as intercumulus phases. Na-clinopyroxene is cotectic with or poikilitic on K-feldspar, amphibole and apatite. Moreover, Na-clinopyroxene occurs as corroded inclusions in amphibole and zoned K-feldspar rims. Rare biotite is found as inclusions in amphibole and K-feldspar.

In leucocratic samples, biotite crystallized as anhedral grains cotectically with alkali feldspar and as inclusions in amphibole. It was replaced to a variable extent by ilmenite + K-feldspar, probably during emplacement at shallow depths. Amphibole occurs as euhedral to acicular and markedly zoned grains. Alkali feldspar is generally inverted to microcline, with exsolved lamellae of hematite, as a result of slow cooling. Acicular apatite, highly variable in abundance, is found as inclusions in alkali feldspar and amphibole. Quartz is a widespread interstitial phase, sometimes occurring as patches. Accessory minerals are zircon, titanite, rutile, Ba- and Nb-titanosilicates.

3.c. Monzodiorite xenolith

A monzodiorite inclusion, some tens of centimetres in size, was partially included and assimilated by the host lamproite. It has hypidiomorphic granular (0.5–1 mm) texture. Pilotaxitic euhedral clinopyroxene, plagioclase, K-feldspar with hematite exsolution in the core and subhedral biotite, likely a high-pressure stage, represent the early-crystallized assemblage. A later stage of crystallization is represented by single feldspar and hornblende overgrown on pyroxene and biotite, likely at lower pressure. Secondary actinolite partially replaces pyroxene and other mafic phases, whereas saussuritization can affect the plagioclase. On the whole, the mineral precipitation in the inclusion

https://doi.org/10.1017/S0016756809990550 Published online by Cambridge University Press

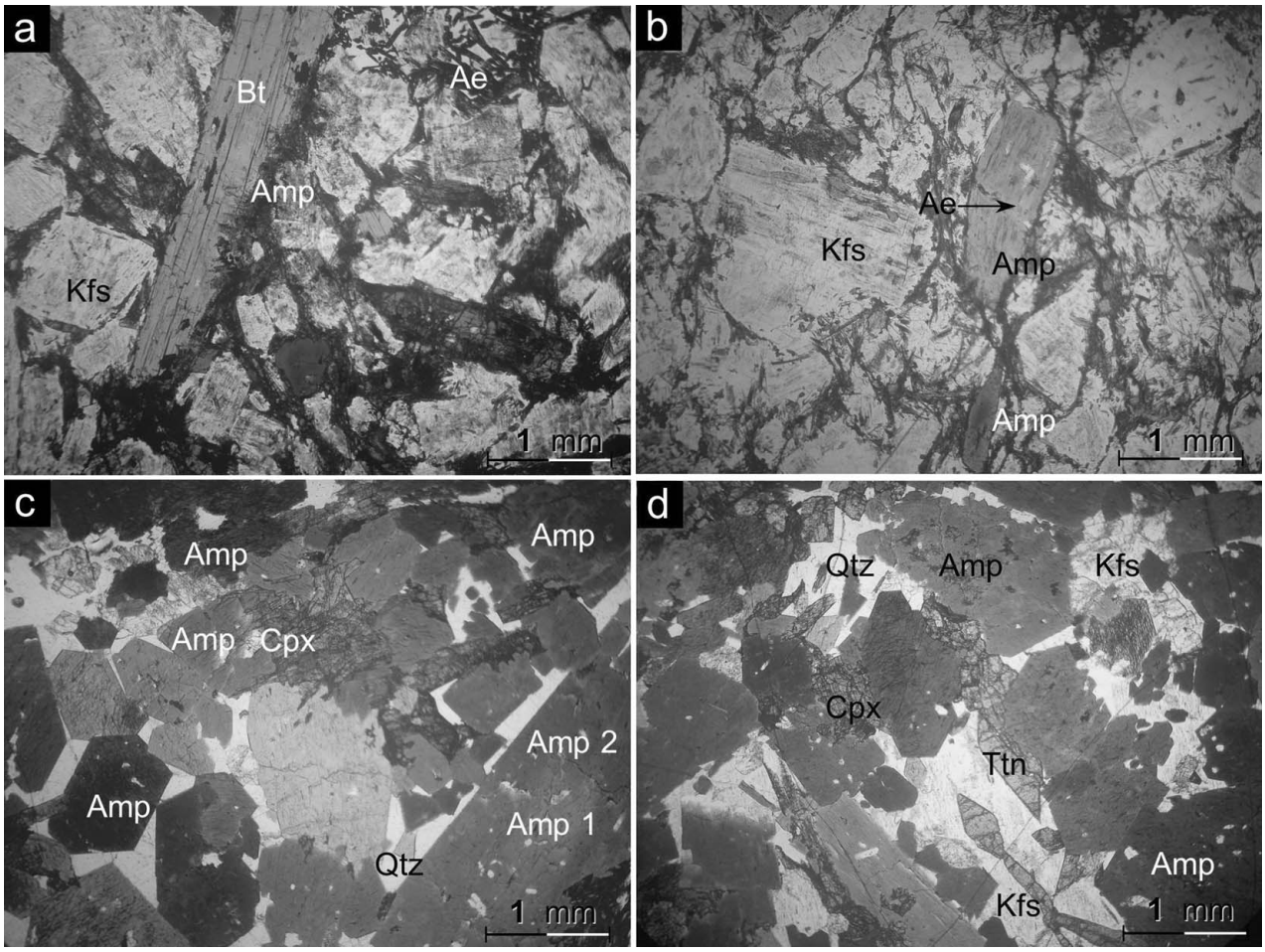

Figure 5. Microphotographs of Svidnya syenites and quartz syenites. Plane polarized light. Scale bar in the photographs. (a) Porphyric alkali feldspar, biotite and aegirine phenocrysts; the groundmass is formed by acicular aegirine, amphibole and K-feldspar. (b) Leucocratic assemblages of K-feldspar and aegirine phenocrysts with interstitial Na-amphibole and acicular aegirine. (c) Orthocumulate texture characterized by euhedral to subhedral zoned amphibole, sometimes poikilitic, cumulus clinopyroxene and intercumulus quartz. (d) Orthocumulate texture characterized by subhedral amphibole, clinopyroxene and titanite as cumulus phases, quartz and K-feldspar as intercumulus phases. For a colour version of this figure see online Appendix at http://journals.cambridge.org/geo.

records the evolution from relatively high- to low-pressure conditions.

4. Analytical methods

Quantitative electron microprobe analyses of mineral phases were acquired using a scanning electron microscope equipped with an X-ray dispersive analyser (EDAX PV9100), installed at the Department for the Study of Territory and its Resources, University of Genoa. Operating conditions were 15 kV accelerating voltage and 2.20 nA beam current. Reference standards for the elements (in brackets) were: jadeite (Na), forsterite (Mg), albite (Al), augite (Si, Ca), microcline (K), ilmenite (Ti), chromite (Cr), rhodonite (Mn) and fayalite (Fe). Other elements were below detection limits. The natural standards were analysed by WDS microprobe at Modena University. Na_2O and MgO contents analysed in silicates by means of an EDAX microprobe are generally underestimated if the analysis is processed with current automatic methods. To overcome this problem, the background for Na (1.040 keV) and Mg (1.252 keV) was manually corrected and considered to be between 0.9 and 4.2 keV. The estimated uncertainties are: 0.1 wt % for SiO_2, TiO_2, Al_2O_3, Cr_2O_3, FeO, MgO, MnO, P_2O_5; 0.05 wt % for CaO and K_2O; 0.25 wt % for Na_2O.

Feldspar analyses, on the basis of eight oxygens, were recalculated to total cations = 5. Clinopyroxene analyses were calculated according to the stoichiometric method of simultaneous normalization to 4 cations and 6 oxygens, and Fe^{3+} = (12 − total cation charge) was considered for clinopyroxene. The allocation of cations to sites T, M1 and M2 was performed according to Morimoto (1988). End-members were calculated in the sequence: wollastonite, enstatite, ferrosilite, aegirine, jadeite, $CaAl_2SiO_6$, $CaFeAlSiO_6$, $CaCrAlSiO_6$ and $CaTiAl_2O_6$. The nomenclature of Morimoto (1988) and Rock (1990) was adopted. The brown mica cation sum was normalized to 7 + Ti − (Na + K) on the basis of 11 oxygens. The amphibole cation sum was normalized to 13 − (Ca + Na + K), as

https://doi.org/10.1017/S0016756809990550 Published online by Cambridge University Press

suggested by Leake *et al.* (1997); Fe^{3+} = (46 − total cation charge); $Fe^{2+} = (Fe_{tot} - Fe^{3+})$; $Al^{IV} = (8 - Si)$; $Al^{VI} = (Al_{tot} - Al^{IV})$. The nomenclature of Leake *et al.* (1997, 2003), revised by Hawthorne & Oberti (2007), was adopted. Mineral abbreviations are after Kretz (1983).

Whole-rock major and trace element abundances for Svidnya ultrapotassic rocks (21 samples) were measured by X-ray fluorescence spectrometry (XRF) at the X-RAL Laboratories (SGS Canada Inc.), Toronto, Canada. Losses on ignition (LOI) were determined by gravimetry. Rare earth elements (REE) were analysed by inductively coupled plasma-mass spectrometry (ICP-MS) at the X-RAL Labs.

Two ^{40}Ar–^{39}Ar age determinations were carried out on amphibole and biotite separates from the lamproite BL42. The separated fractions (95 % amphibole and 5 % biotite) were analysed by ^{40}Ar–^{39}Ar incremental heating at the Actlab Laboratories (Canada). The samples wrapped in Al foil were loaded in evacuated and sealed quartz vials with K and Ca salts and packets of LP-6 biotite interspersed with the samples to be used as a flux monitor. The samples were irradiated in a nuclear research reactor for 24 hours. The flux monitors were placed between every two samples, thereby allowing precise determination of the flux gradients within the tube. After the flux monitors were run, J values were calculated for each sample, using the measured flux gradient. The neutron gradient did not exceed 0.5 % of sample size. LP-6 biotite has an assumed age of 128.1 Ma.

Sample dissolution and isotopic analysis were carried out at the Earth Science Department, University of Trieste. Samples were dissolved for isotopic analysis in Teflon® vials using a mixture of HF–HNO_3 and HCl purified reagents. Sr and Nd were collected after ion exchange and reversed-phase chromatography, respectively; total blank for Sr was less than 20 pg. The Sr and Nd isotopic compositions were obtained using a VG 54E mass spectrometer and 'Analyst' software (Ludwig, 1994) for data acquisition and reduction. The $^{87}Sr/^{86}Sr$ and $^{143}Nd/^{144}Nd$ were corrected for fractionation to $^{86}Sr/^{88}Sr = 0.1194$ and $^{146}Nd/^{144}Nd = 0.7219$, respectively, and the measured ratios were corrected for instrumental bias to NBS 987 and La Jolla standard values of 0.71025 ± 0.00002 (n = 12) and 0.511860 ± 0.000021 (n = 9). The reported errors represent statistics at the 95 % confidence level. Neodymium-model ages were calculated with respect to a depleted mantle evolution curve given by $\varepsilon Nd(T) = 0.25T^2 - 3T + 8.5$ (T in Ga) as reported in Ludwig (1994).

5. Mineral chemistry

5.a. Feldspars

Lamproites are characterized by euhedral Fe-rich K-sanidine (FeO up to 0.6 wt %) with $Or_{97–99}$. Na-richer (Or_{65}) sanidine/amphibole intergrowths rarely occur. Melasyenites contain Ba-rich sanidine ($Or_{88}Cel_{12}$), and perthitic anorthoclase ($Ab_{97}Or_2An_1$) and sanidine ($Or_{96}Ab_3$).

In the monzodiorite inclusion, plagioclase as inclusion in K-feldspar evolves from early-crystallized andesine to oligoclase.

In syenites and quartz syenite, K-feldspar is homogeneous, with high Fe and low Na and Ba contents.

5.b. Clinopyroxene

The early-crystallized clinopyroxene in lamproite (Fig. 4a; Table 2; Fig. A1 in online Appendix at http://journals.cambridge.org/geo) is Al- and Ti-poor ($TiO_2 < 0.8$ wt %) diopsidic-augite, a typical feature of clinopyroxene in lamproites (Conticelli, 1998), with increasing aegirine solid solution towards the rim (Ae_5). Fine-grained groundmass crystals are augite to aegirine-augite. Corroded clinopyroxene, overgrown by amphibole, has a higher aegirine content (up to 24 mol. %). Diopsidic-augite ($Ae_{5–14}$) to aegirine (up to Ae_{76}) precipitates in melasyenites.

In the monzodiorite, pyroxenes are diopsides with relatively high-Al cores (Fig. 4a). Early-crystallized aegirine-augite up to acicular aegirine occurs in syenites and quartz syenite.

5.c. Mica

Micas from lamproites (Table 3) are solid solutions between the phlogopite and annite end-members, characterized by high titanium contents (1.29–6.28 wt % TiO_2). Rarely they show weak zoning, that is, a core-to-rim MgO increase at decreasing FeO, Al_2O_3 and TiO_2. A reversed zoning profile was observed in biotites from melasyenites (Fig. 4b).

Biotites from the monzodiorite inclusion and the rounded aggregates in olivine-lamproites are Al-rich (> 13 wt % Al_2O_3) with significant eastonite solid solution (Fig. 4b).

In syenites and quartz syenite, micas are relatively homogeneous solid solutions between predominant phlogopite and subordinate annite end-members.

5.d. Amphibole

The sodic–calcic amphiboles from lamproites (Table 4) are mostly richterite, magnesiokatophorite and winchite (Leake *et al.* 1997, 2003; Hawthorne & Oberti, 2007). Rarely, their rims evolve to ferri-glaucophane. In melasyenites, from core to rim the amphiboles grade from richterite/winchite to ferri-eckermannite and ferri-glaucophane. The amphiboles from monzodiorite inclusions have magnesiohornblende compositions with an exceptionally high Al_2O_3 content (up to 6.7 wt %).

In syenites the early-crystallized amphiboles are richterite and winchite, rimmed by ferri-eckermannite, eckermannite and, finally, ferri-glaucophane.

https://doi.org/10.1017/S0016756809990550 Published online by Cambridge University Press

Table 2. Selected electron microprobe analyses of clinopyroxenes

Lithology	Lamproite			Melasyenite		Xenolith		Syenite		
Sample	BL55	BL56	BL44	B39B	B39B	G54	G54	B39A	B39A	B36
Classification	Augite	Augite	Augite	Aegirine-augite	Aegirine-augite	Augite	Augite	Aegirine	Aegirine	Aegirine-augite
Occurrence	Core	Rim	Interstitial	Core	Rim	Core	Rim	Core	Rim	Acicular
Oxide (wt %)										
SiO_2	53.5	52.8	53.1	52.8	53.0	52.1	51.9	53.5	53.5	52.8
TiO_2	0.3	0.9	0.4	0.6	1.2	0.2	0.2	5.7	4.9	4.8
Cr_2O_3	0.3	0.3	0.3	0.3	0.5	0.1	0.3	0.2	0.2	0.0
Al_2O_3	0.3	0.2	0.1	0.1	0.2	1.2	0.5	0.3	0.1	0.5
FeO_{tot}	6.1	10.3	8.6	21.0	22.9	10.8	11.3	22.7	23.2	20.5
MnO	0.2	0.4	0.5	0.3	0.4	0.5	0.5	0.4	0.4	0.6
MgO	14.9	13.1	14.9	5.6	3.4	12.9	11.8	2.0	1.9	3.3
NiO	0.0	0.1	0.0	0.1	0.1	0.0	0.0	0.1	0.1	0.4
CaO	23.1	19.6	21.2	10.5	6.5	22.2	23.2	1.2	1.7	2.5
Na_2O	0.7	2.1	0.0	8.8	10.3	0.0	0.0	13.1	13.2	13.8
K_2O	0.2	0.2	0.2	0.2	0.3	0.2	0.2	0.2	0.2	0.1
Total	99.7	99.8	99.3	100.2	98.6	100.2	99.8	99.2	99.3	99.3
Cations										
Si	1.976	1.961	1.993	1.951	1.995	1.957	1.970	1.993	1.986	1.957
Ti	0.009	0.025	0.011	0.017	0.034	0.006	0.004	0.159	0.136	0.075
Cr	0.010	0.009	0.008	0.010	0.015	0.004	0.008	0.004	0.006	0.006
Al	0.012	0.007	0.006	0.004	0.007	0.054	0.021	0.012	0.006	0.000
Fe^{3+}	0.069	0.173	0.000	0.648	0.680	0.024	0.033	0.631	0.703	0.634
Fe^{2+}	0.120	0.148	0.270	0.000	0.042	0.316	0.325	0.076	0.017	0.000
Mn	0.007	0.012	0.016	0.008	0.012	0.015	0.016	0.011	0.014	0.013
Mg	0.821	0.723	0.833	0.310	0.189	0.723	0.666	0.108	0.107	0.269
Ni	0.000	0.002	0.000	0.002	0.004	0.000	0.001	0.004	0.003	0.001
Ca	0.914	0.782	0.853	0.415	0.262	0.894	0.945	0.050	0.068	0.313
Na	0.052	0.150	0.000	0.628	0.749	0.000	0.000	0.945	0.948	0.723
K	0.009	0.010	0.011	0.008	0.013	0.007	0.011	0.007	0.008	0.009
End-members										
Wollastonite	0.454	0.389	0.425	0.207	0.129	0.428	0.464	0.023	0.033	0.156
Enstatite	0.411	0.363	0.417	0.156	0.096	0.362	0.333	0.056	0.055	0.135
Ferrosilite	0.060	0.074	0.135	0.000	0.021	0.158	0.163	0.038	0.008	0.000
Pyroxmangite	0.003	0.006	0.008	0.004	0.006	0.007	0.008	0.006	0.007	0.007
Aegirine	0.062	0.159	0.000	0.635	0.680	0.007	0.011	0.631	0.703	0.634
Jadeite	0.000	0.000	0.000	0.000	0.002	0.000	0.000	0.005	0.000	0.000
$CaTiAl_2O_6$	0.006	0.004	0.003	0.002	0.003	0.006	0.004	0.003	0.002	0.000

Table 3. Selected electron microprobe analyses of micas

Lithology	Lamproite			Melasyenite				Xenolith
Sample	B39C		BL36	B39B		B38		G54
Occurrence	Core	Rim	Core of the patches	Core	Rim	Corona on olivine	Poikilitic phenocryst	Euhedral
Oxides (wt %)								
SiO_2	38.2	42.1	34.4	38.3	38.8	40.1	39.9	36.1
TiO_2	4.3	1.3	3.8	4.9	5.1	3.2	4.8	4.1
Cr_2O_3	0.3	0.2	0.1	0.1	0.2	0.1	0.2	0.1
Al_2O_3	11.1	9.7	14.2	8.9	9.1	10.7	10.3	14.8
FeO_{tot}	19.2	16.1	20.7	19.6	20.0	14.2	17.1	20.9
MnO	0.4	0.3	0.4	0.3	0.4	0.3	0.3	0.3
MgO	12.7	17.3	11.4	13.8	13.5	17.2	15.3	11.4
NiO	0.1	0.1	0.3	0.1	0.1	0.1	0.1	0.0
CaO	0.2	0.4	0.1	0.0	0.0	0.3	0.2	0.1
Na_2O	0.0	0.0	0.2	0.0	0.0	0.0	0.0	0.0
K_2O	10.1	9.1	9.5	9.9	9.9	9.6	10.0	9.8
Total	96.5	96.4	95.0	96.0	97.0	95.6	98.1	97.5
Cations								
Si	2.866	3.097	2.681	2.866	2.871	2.946	2.890	2.675
Ti	0.241	0.071	0.220	0.275	0.282	0.174	0.259	0.227
Cr	0.015	0.012	0.008	0.004	0.011	0.006	0.011	0.008
Al	0.981	0.837	1.302	0.788	0.795	0.927	0.875	1.291
Fe^{3+}	0.277	0.046	0.032	0.530	0.512	0.228	0.376	0.402
Fe^{2+}	0.927	0.944	1.321	0.699	0.724	0.646	0.659	0.892
Mn	0.025	0.016	0.023	0.018	0.025	0.016	0.020	0.017
Mg	1.420	1.899	1.324	1.541	1.495	1.880	1.647	1.261
Ni	0.005	0.006	0.013	0.005	0.003	0.003	0.004	0.000
Ca	0.015	0.030	0.010	0.000	0.003	0.024	0.017	0.010
Na	0.000	0.000	0.045	0.000	0.000	0.000	0.000	0.000
K	0.964	0.850	0.946	0.948	0.934	0.898	0.924	0.928

https://doi.org/10.1017/S0016756809990550 Published online by Cambridge University Press

Table 4. Selected electron microprobe analyses of amphiboles

Lithology	Lamproite		Melasyenite		Xenolith	Syenite		
Sample	BL55	BL55	G29		G54	G56	XX	XX
Classification Occurrence	Richterite Overgrowth on Cpx	Mg-Ktp	Richterite Core	Ferri-eck Rim	Mg-Hbl Core	Richterite	Richterite Core	Ferri-eck Rim
Oxide (wt %)								
SiO_2	54.7	51.6	53.2	53.3	49.8	53.7	52.2	54.8
TiO_2	0.9	2.3	1.7	2.8	0.7	2.6	2.9	2.5
Cr_2O_3	0.2	0.2	0.1	0.1	0.1	0.3	0.0	0.0
Al_2O_3	0.2	1.6	1.2	1.2	4.9	0.5	1.4	0.6
FeO_{tot}	13.5	12.8	10.3	19.1	16.5	14.4	9.4	12.9
MnO	0.4	0.4	0.3	0.3	0.5	0.4	0.3	1.3
MgO	16.2	16.0	16.9	10.3	12.6	13.3	17.1	14.3
NiO	0.0	0.3	0.0	0.0	0.0	0.0	0.1	0.2
CaO	7.2	6.7	6.6	2.5	12.3	4.1	6.1	1.5
Na_2O	3.9	4.6	4.8	6.6	0.0	6.1	5.0	7.8
K_2O	0.8	1.9	2.7	1.4	0.5	2.8	2.9	2.7
Total	98.1	98.4	97.7	97.5	97.9	98.1	97.4	98.5
Cations								
Si	7.766	7.413	7.699	7.833	7.261	7.873	7.557	7.860
Ti	0.098	0.243	0.187	0.306	0.076	0.287	0.318	0.265
Al^{IV}	0.037	0.278	0.198	0.167	0.739	0.092	0.246	0.093
Al^{VI}	0.000	0.000	0.000	0.050	0.101	0.000	0.000	0.000
Cr	0.018	0.019	0.009	0.007	0.014	0.029	0.000	0.000
Fe^{3+}	0.727	0.646	0.126	0.371	0.479	0.020	0.160	0.479
Fe^{2+}	0.878	0.894	1.114	1.979	1.533	1.741	0.977	1.067
Mn	0.048	0.046	0.033	0.032	0.061	0.052	0.038	0.158
Mg	3.428	3.432	3.633	2.255	2.737	2.901	3.695	3.058
Ni	0.000	0.029	0.001	0.000	0.000	0.005	0.009	0.020
Ca	1.119	1.050	1.024	0.388	1.947	0.648	0.955	0.239
Na_B	0.782	0.883	0.976	1.612	0.000	1.352	1.045	1.761
Na_A	0.315	0.403	0.369	0.262	0.000	0.372	0.355	0.441
K	0.155	0.359	0.501	0.476	0.100	0.520	0.536	0.496

6. Crystallization temperature of the xenolith assemblages

The andalusite–biotite pair in the country rock places the upper pressure limit for emplacement of the Svidnya main intrusion at 0.37 ± 0.02 GPa (Spear & Cheney, 1989).

Plagioclase–amphibole thermometry (Holland & Blundy, 1994) was only possible in the monzodiorite inclusion, where rims of hornblendes and plagioclases yielded temperatures in the range 741–685 °C for a likely maximum pressure of 0.4 GPa, and 766–706 °C for a pressure of 0.2 GPa.

The two-feldspar geothermometer of Fuhrman & Lindsley (1988) for coexisting alkali feldspar and plagioclase in the xenolith assemblage, yielded a temperature of 787–780 °C for pressures between 0.5 and 0.4 GPa. The pressure interval was assumed on the stability curve of biotite (Wones & Eugster, 1965; Huebner & Sato, 1970; Wones, 1972) and is consistent with experimental results for the stability of Fe–Al biotites (Rutherford, 1973). Based on this, Buda & Dobosi (2004) suggest 800 °C and 0.5 GPa for the crystallization of Mg-rich biotites from high-K mafic enclaves within Variscan granitoids.

The equilibration temperatures were determined with the SOLVCALC 1.0 software of Wen & Nekvasil (1994), using the feldspar site mixing model of Fuhrman & Lindsley (1988) with assessed uncertainties of ± 30 °C. Temperatures were calculated for pressures between 0.5 and 0.4 GPa at a compositional uncertainty of 0.020 (molar end-member composition). The result is a smooth curve with temperature rising with pressure at about 7 °C per 0.1 GPa.

By using the two-feldspar geothermometer, and based on the crystallization order, the near-solidus temperatures can be estimated at about 555–493 °C for pressures between 0.2 and 0.4 GPa, and correspond to the final stage of crystallization of the inclusion, in accordance with data from the Buhovo-Seslavtzi peralkaline rocks (Dyulgerov & Platevoet, 2006).

7. Geochemistry

The Svidnya main intrusion, according to Le Bas *et al.* (1986), is peralkaline (molar $(K+Na)/Al > 1.0$, Table 5) and generally perpotassic (molar K/Al between 0.6 and 1.0). Following Foley *et al.* (1987), it may be considered ultrapotassic ($MgO > 3$ wt %; $K_2O > 3$ wt % and $K_2O/Na_2O > 3$). On the basis of chemical analyses by Stefanova (1966), Foley *et al.* (1987) referred the Svidnya main intrusion to group IV of ultrapotassic rocks, transitional between lamproites, kamafugites and rocks of orogenic areas. However, they plot in the lamproite field in the K_2O, MgO and Al_2O_3 classification diagram (Fig. 6a; Bergman, 1987), as well as in the Foley *et al.* (1987) variation diagrams (Fig. A2 in online Appendix at http://journals.cambridge.org/geo). The normative classification of syenite plugs and dykes is consistent with alkali-feldspar syenite and alkali-feldspar quartz syenite (Fig. 6b).

https://doi.org/10.1017/S0016756809990550 Published online by Cambridge University Press

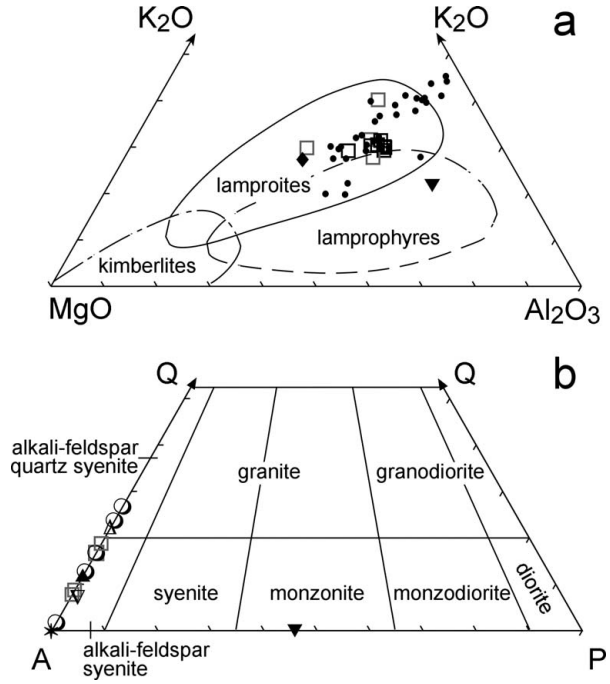

Figure 6. Whole rock classification diagrams. Small circles are literature data of Svidnya ultrapotassic rocks (Vladykin, Grozdanov & Bonev, 2001). (a) K_2O, MgO and Al_2O_3 classification diagram for lamproites (Bergman, 1987). (b) CIPW normative AQP composition of syenites (Le Bas & Streckeisen, 1991). For legend see Figure 4.

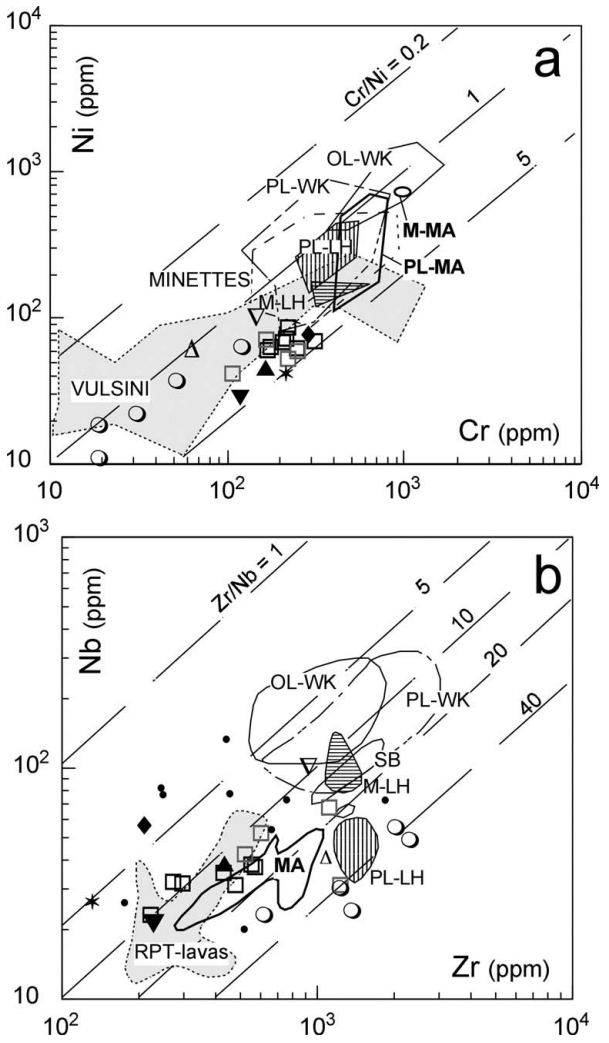

Figure 7. Binary correlations: (a) Ni v. Cr; (b) Nb v. Zr. Data source from Mitchell & Bergman (1991). Compositional fields are: M-LH – madupitic lamproite Leucite Hills; M-MA – madupitic lamproite Murcia Almeria; OL-WK – olivine lamproite West Kimberley; PL-LH – phlogopite lamproite Leucite Hills; PL-MA – phlogopite lamproite Murcia Almeria; PL-WK phlogopite lamproite West Kimberley; RPT-lavas – Roman-province-type lavas; SB – Smoky Butte lamproite. For legend see Figure 4.

The lamproites are silica-saturated with SiO_2 in the range 49.7–56.4 wt %, Mg-number up to 44, Al_2O_3 contents between 10.7 and 12 wt %, TiO_2 about 1.3 wt %, Cr and Ni up to 309 and 86 ppm, respectively (Fig. 9a; Table 5). Melasyenites have higher SiO_2 contents, up to 60.8 wt %, Mg-number from 33 to 47, Al_2O_3 between 6.2 and 10.5 wt %, TiO_2 in the range 1.0–1.5 wt %, Cr and Ni abundances are lower than 250 and 70 ppm, respectively (Fig. 9a).

Compared with anorogenic lamproites, the Svidnya lamproites and melasyenites are characterized by: (1) higher Ba/Sr (in the range 4.5–6.7) than Roman Province-type (RPT) lavas (0.5–2.0), kimberlites, alkali basalts, lamprophyres (1–1.4) and primitive mantle (0.3); (2) significantly higher Zr/Nb (7.5–18.3) than kimberlites, alkali basalts and lamprophyres (0.4–4), but similar to primitive mantle (13) and (3) lower Ni contents and Nb/Th (0.2–1.0).

On the whole, SiO_2, low TiO_2, low Ni and Nb/Th make the Svidnya main intrusion similar to orogenic ultrapotassic lavas ($TiO_2 < 2$ wt %; Foley *et al.* 1987) and to Mediterranean Cenozoic lamproites (Prelevic *et al.* 2008; Fig. 7a, b), particularly the peralkalic Sisco, Corsica (Conticelli *et al.* 2002) and Cancarix and Calaspara, Spain (Prelevic *et al.* 2008) examples. Compared with Carboniferous Mg–K granites from the French Central Massif, Svidnya lamproites have lower SiO_2 and higher TiO_2, but similar $MgO/(MgO + FeO_t)$ and $K_2O/K_2O + Na_2O$ (Sabatier, 1980; Fig. A3 in online Appendix at http://journals.cambridge.org/geo).

The Svidnya lamproites and melasyenites show homogeneous REE distribution patterns normalized to chondrite (Sun & McDonough, 1989; Fig. 8a) with lower REE abundances (ΣREE in the range 317–477; Table 6) and very low La/Yb ($15 < La_N/Yb_N < 24$) compared with anorogenic lamproites. They show a weak negative Eu anomaly (Eu/Eu^* on average 0.59), as in the Sisco lamproites, and patterns similar to those of the Murcia–Almeria lamproites. The monzodiorite inclusion shows higher ΣREE than the host rocks, with Eu negative anomaly and HREE fractionation. The syenite and quartz syenites are characterized by ΣREE in the range 142–591, with evident HREE fractionation ($14 < La_N/Yb_N < 50$) and small negative Eu anomaly (Eu/Eu^* on average 0.61; Fig. 8b).

The multi-element diagram normalized to primitive mantle (Sun & McDonough, 1989; Fig. 9a) shows a

https://doi.org/10.1017/S0016756809990550 Published online by Cambridge University Press

Table 5. Whole rock major (%) and trace element (ppm) analyses

Lithology	Lamproite			Melasyenite	Monzodiorite xenolith	Syenite		Qtz-syenite		Melanocratic syenite		Leucocratic Qtz-syenite
Sample	BL43	BL44	BL55	BL49	G54	N79	B37	BL47	G44	G5	G36	BL40
Oxides (wt %)												
SiO_2	52.62	49.71	52.83	57.63	50.12	59.90	62.30	66.91	62.52	55.55	51.20	65.30
TiO_2	1.27	1.56	1.25	1.02	1.12	1.38	1.19	0.88	0.89	1.39	0.85	0.74
Al_2O_3	11.98	10.71	11.44	10.19	6.51	9.68	10.20	9.87	9.64	8.34	15.77	13.40
Fe_2O_3	8.27	9.62	7.89	6.77	8.27	10.30	7.63	7.01	7.03	9.54	7.22	4.97
Cr_2O_3	0.03	0.04	0.03	0.03	0.04	0.02	0.02	0.01	0.01	0.02	0.02	0.01
CaO	5.07	6.15	5.64	4.43	9.72	1.39	1.36	0.74	0.71	2.86	6.39	0.97
MgO	5.97	7.55	6.21	5.46	8.19	4.09	1.94	1.10	1.08	5.10	4.48	0.47
MnO	0.21	0.24	0.16	0.17	0.21	0.15	0.19	0.11	0.12	0.25	0.15	0.10
Na_2O	2.33	1.88	2.60	3.42	3.54	4.03	3.99	4.42	3.38	4.24	2.82	0.67
K_2O	7.89	7.54	7.68	7.25	5.40	7.72	8.26	8.13	7.08	7.31	5.55	10.70
P_2O_5	1.51	1.99	1.70	1.50	4.44	0.51	0.42	0.19	0.16	1.19	0.89	0.72
LOI	1.68	1.83	1.53	0.82	1.15	0.60	0.70	0.77	0.50	1.00	1.55	1.15
Sum	98.83	98.82	98.93	98.67	98.71	99.77	98.20	100.14	93.12	96.79	96.89	99.20
Trace elements (ppm)												
Ba	3580	3380	3825	3395	2670	2140	3520	2610	1740	1820	1990	2010
Co	47.4	49.2	47.1	54.4				39.5				
Cr	246	309	205	220	251	121	52	18	19	128	118	63
Cs	22.4	24	26.8	7.8				9.4				
Hf	11	7	8	13	4			49	28	25	6	
Nb	35	32	31.5	52	55	30	55	42	24	99	21	42
Ni	62	69	68	52.5	74	63	37	13	11	98	28	60
Rb	409	402	374	300.5	189	293	377	373	285	276	320	458
Sc	24	29	27	18				< 10				
Sr	671	630	748	750.5	1960	415	930	167	161	1140	692	326
Ta	2	1.8	1.7	5.6	2.8			3.5	2.4	7.6	1.4	
Th	49.3	53.2	37.3	94	146	78.7	613	259	409	194	26.4	55
U	12.2	12	9.1	21	21.7	14.7	67.6	37	44.9	27	13.9	30.2
V	162	173	156	122	233			91	51	185	92	
W	195	174	174	319				331				
Y	26.6	28.4	36.1	39.05	54.6	22	41	11.7	12	62.8	14.7	33
Zn	105	89	97	117				85				
Zr	428	272	296	601	192	1230	2030	1790	1370	846	228	1080

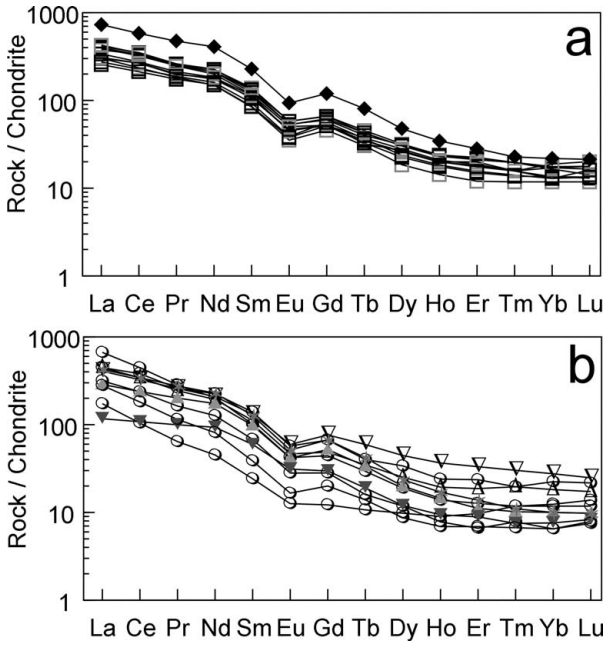

Figure 8. Chondrite normalized REE-patterns (Sun & McDonough, 1989) for (a) lamproites and monzodiorite intrusion, (b) syenites and quartz syenites. For legend see Figure 4.

common LILE enrichment with HFSE fractionation, Nb, Ta, Sr, and Ti troughs, Th and U spikes. Syenites and quartz syenites show strongly variable Th, U, Hf and Zr abundances, and Nb, Ta, Sr and Ti troughs (Fig. 9b). Fractionated syenites tend to be Zr- and Hf-enriched.

8. Emplacement age

8.a. Results

Two ^{40}Ar–^{39}Ar age determinations were carried out on amphibole and biotite separates from the lamproite BL42.

The argon release spectra are given in Figure 10. The biotite fraction (Fig. 10a) yielded a plateau age of 339.1 ± 1.6 Ma for 79.9 % of the released ^{39}Ar. The total fusion age is 335.1 ± 3.1 Ma and is therefore concordant with the plateau age.

The amphibole fraction (Fig. 10b) yielded a near-plateau age of 337 ± 4 Ma. At lower temperatures the oldest age of 365.5 ± 36.3 Ma represents almost 0.5 % of the released gas. A cluster of $^{40}Ar/^{39}Ar$ increments contributes to about 16 % of the released gas. This cluster corresponds to the youngest and apparent ages, and approaches the total fusion age (313 ± 3 Ma). Two following incremental heating steps correspond to 337 ± 4 Ma for 35 % of the gas released. At higher temperatures, ages drop to 303 ± 3 Ma and then again rise to 336 ± 4 Ma, that is, 24.9 and 10.1 % of the released gas, respectively.

https://doi.org/10.1017/S0016756809990550 Published online by Cambridge University Press

Table 6. Whole rock rare earth element concentrations (ppm)

Lithology	Lamproite			Melasyenite	Monzodiorite xenolith	Syenite		Qtz-syenite		Melanocratic syenite		Leucocratic Qtz-syenite
Sample	BL43	BL44	BL55	BL49	G54	N79	B37	BL47	G44	G5	G36	BL40
REE (ppm)												
La	60.7	65	91.1	85.4	173	158	106	37.2	66.2	96.3	27.7	106
Ce	130	139	198	193	355	273	233	59.9	111	199	66.1	210
Pr	16.6	17.9	23.9	24.1	45	27	24.8	5.96	10.9	24.6	9.47	23.2
Nd	70.5	74.9	100.2	103	191	94.6	105	20.7	37.9	97.5	43.6	90.5
Sm	13.1	14.3	19.5	21.3	34.9	15.5	21.3	3.7	5.9	20.1	9.1	17.1
Eu	2.19	2.25	3.11	3.24	5.41	2.44	3.32	0.49	0.96	3.45	1.81	2.69
Gd	10.6	11.6	13.6	14.5	24.6	9.1	13.7	2.68	4.12	15.7	6.1	10
Tb	1.23	1.37	1.65	1.76	3.02	1.1	1.5	0.39	0.52	2.22	0.71	1.3
Dy	5.72	6.02	7.33	8.39	12.1	4.8	8.6	1.92	2.2	11.3	3.04	6.4
Ho	1	1.04	1.28	1.39	1.95	0.78	1.36	0.39	0.39	2.07	0.53	1.1
Er	2.49	2.58	3.27	3.68	4.66	2.1	3.9	1.28	1.15	5.5	1.48	3.1
Tm	0.35	0.36	0.47	0.49	0.58	0.3	0.5	0.22	0.17	0.77	0.19	0.5
Yb	2.3	2.2	2.65	3.05	3.7	2.1	3.8	1.7	1.1	4.7	1.3	3.1
Lu	0.34	0.41	0.38	0.43	0.54	0.35	0.55	0.25	0.19	0.63	0.21	0.44
La_N/Sm_N	2.99	2.93	3.01	2.59	3.20	6.29	3.21	6.20	7.24	3.09	1.88	4.00
Gd_N/Yb_N	3.81	4.36	4.25	3.92	5.50	3.45	2.98	1.26	3.10	2.76	3.74	2.67
La_N/Yb_N	18.9	21.2	24.6	20.1	33.5	50.3	20.0	14.6	43.2	14.7	14.2	24.5
ΣREE	317	339	466	463	855	591	527	137	243	484	171	475
Eu/Eu*	0.57	0.53	0.58	0.56	0.56	1.05	0.59	0.26	0.60	0.59	0.89	0.63
ΣLREE	278	297	413	405	764	553	469	124	226	417	147	430
ΣHREE	5.48	5.55	6.77	7.64	9.48	4.85	8.75	3.45	2.61	11.60	3.18	7.14

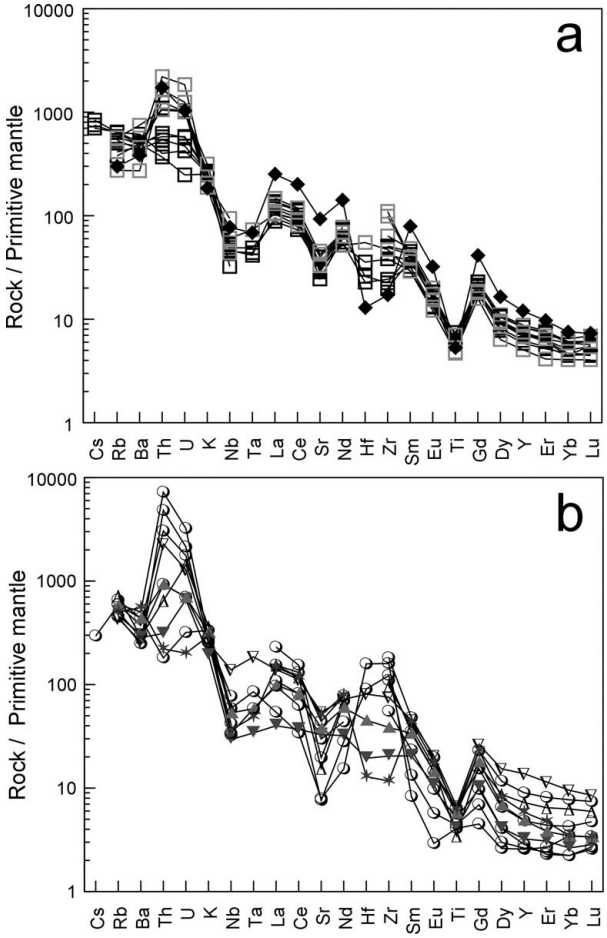

Figure 9. Primitive mantle-normalized multi-element diagram (Sun & McDonough, 1989) for (a) lamproites and monzodiorite intrusion, (b) syenites and quartz syenites. For legend see Figure 4.

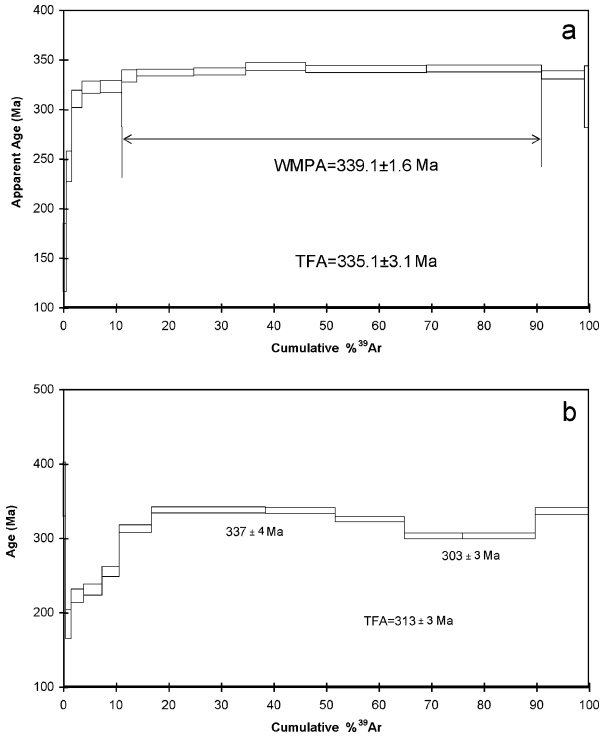

Figure 10. $^{40}Ar/^{39}Ar$ incremental release spectra for biotite (a) and amphibole (b) of the Svidnya lamproites (sample BL42).

While the apparent ages for both fractions overlap within uncertainties, the total fusion ages for the amphibole and biotite fractions are slightly different.

8.b. Interpretation

The age spectrum for the biotite fraction indicates a homogeneous argon isotopic content and implies that the biotite was essentially closed to argon diffusion after cooling. We interpret the plateau age of 339.1 ± 1.6 Ma as the cooling age through the biotite Ar-retention temperature.

The ^{40}Ar–^{39}Ar release spectrum obtained from the amphibole fraction indicates heterogeneity in the argon isotopic composition of the sample; however, the high temperature steps yielded geologically meaningful

https://doi.org/10.1017/S0016756809990550 Published online by Cambridge University Press

Table 7. Whole rock Sr and Nd isotope data

Lithology	Sample	$^{87}Rb/^{86}Sr$	$^{87}Sr/^{86}Sr$ ($\pm 2\sigma$)	$(^{87}Sr/^{86}Sr)_i$	$\varepsilon(Sr)_i$	$^{147}Sm/^{144}Nd$	$^{143}Nd/^{144}Nd$ ($\pm 2\sigma$)	$(^{143}Nd/^{144}Nd)_i$	$\varepsilon(Nd)_i$
Lamproite	BL43	1.765	0.71599	0.70752	48.50	0.112	0.51216	0.51191	−5.80
Lamproite	BL55	1.398	0.71439	0.70769	50.80	0.120	0.51222	0.51195	−4.87
Melasyenite	BL49	1.218	0.71278	0.70694	40.19	0.127	0.51218	0.51190	−5.88
Monzodiorite xenolith	G54	0.279	0.70960	0.70826	58.98	0.111	0.51217	0.51193	−5.41
Syenite	N79	2.048	0.73478	0.72496	296.07	0.099	0.512392	0.51217	−0.60
Qtz-syenite	G44	5.138	0.73949	0.71485	152.50	0.094	0.51235	0.51214	−1.25
Qtz-syenite	BL47	6.481	0.73718	0.70609	28.17	0.108	0.51212	0.51188	−6.24
Leucocratic Qtz-syenite	BL40	4.073	0.72790	0.70836	60.43	0.114	0.51219	0.51194	−5.16
Melanocratic syenite (Am-Ae-Ap cumulus)	G36	1.339	0.71544	0.70902	69.72	0.126	0.51218	0.51190	−6.01
Melanocratic syenite (Cpx-Bt cumulus)	G5	0.701	0.71160	0.70824	58.66	0.125	0.51215	0.51188	−6.35
Southern Hungary (Buda & Dobosi, 2004)				0.7080–0.7087					−5.20
Bohemian Massif (Gerdes, Wöerner & Finger, 2000)				0.7062–0.7090					−2.6 to −5.2

Initial Sr and Nd are recast to 339 Ma (^{40}Ar–^{39}Ar dating on biotite, present work).

ages. The gas extracted at high temperature reflects the amphibole degassing, whereas low temperature steps, which account for < 18 % of the total Ar, record the chemical signature (Ca/K, Cl/K) of contaminating phases. Moreover, amphibole is strongly susceptible to contamination due to potassium contents lower than other potassium phases such as micas (Wartho, 1995). At intermediate-high temperatures, the deviations in Ca/K and Cl/K (derived from Ar isotopes) are decoupled from the step ages, suggesting that the mixture of different minerals is an unlikely hypothesis (Villa *et al.* 1996). Meanwhile, the veining by syenite and quartz syenite across the lamproite intrusion likely affected the thermal equilibrium. Thus the younger incremental age of 303 ± 3 Ma for the amphibole fraction likely reflects a chemical re-equilibration of richterite during this later thermal event, which may result in partial ^{40}Ar loss. This is supported by the petrographic evidence of actinolite forming on the rims of diopside and richterite grains.

The biotite total-fusion age is consistent with a K–Ar age of 340 Ma on biotite (Lilov, Grozdanov & Peeva, 1968) and a Pb age of 330 ± 10 Ma on K-feldspar and galena from ultrapotassic rocks from the Svoge region (Stefanova, Pavlova & Amov, 1974).

9. Sr–Nd isotopic data

9.a. Lamproites

The measured $^{87}Sr/^{86}Sr$ and $^{143}Nd/^{144}Nd$ range from 0.71278 to 0.71599 and 0.512155 to 0.512219 in lamproites and melasyenites (Table 7). The Nd and Sr isotope ratios were corrected back to 339 Ma on the basis of the ^{40}Ar–^{39}Ar dating on biotite (Fig. 11). The initial ε_{Nd} values range between −4.87 and −5.88, suggesting a source relatively enriched in LREE with respect to Bulk Earth. The Nd model ages calculated (Ludwig, 1994) with respect to a depleted source (initial εNd between +4.4 and +5.0) range between 1.3 and 1.5 Ga, thus representing the age of the enrichment event, assuming a pristine depleted mantle source. The relatively radiogenic Sr isotopic composition ($^{87}Sr/^{86}Sr_i = 0.70694$–$0.70769$) agrees with a time-integrated enriched mantle source. Despite the restricted dataset, the lack of a positive correlation of $^{87}Sr/^{86}Sr$ with lithophile elements, the enrichment of most incompatible elements (e.g. Ti, Th, Nb, La), and high Cr and Ni compared with continental crust abundances (Rudnick & Gao, 2004) suggest that crustal contamination alone is insufficient to account for the radiogenic signature of these magmas. The isotopic data are instead consistent with an origin of lamproites from a depleted mantle, contaminated by an enriched component, probably related to metasomatic processes by sediment dehydration during an ancient subduction event. In addition, the Sr and Nd isotope compositions of the Kfs–Cpx–Plg–Bt–Hbl-bearing monzodiorite inclusion and of its host rock, suggest a common origin from the same mantle source.

9.b. Syenite

The initial $^{87}Sr/^{86}Sr$ and ε_{Nd} values range from 0.70609 to 0.72496 and −6.24 to −0.60, respectively (Fig. 11; Table 7). In particular, four samples are characterized by initial values similar to those in lamproites. Nevertheless, two samples show a markedly different ε_{Nd}, approaching a Bulk Earth signature and slightly enriched ($\varepsilon_{Nd} = -0.60$ and -1.24). These samples are also characterized by an unusually radiogenic Sr signature, which appears to be decoupled with respect to the corresponding Nd isotopic composition.

https://doi.org/10.1017/S0016756809990550 Published online by Cambridge University Press

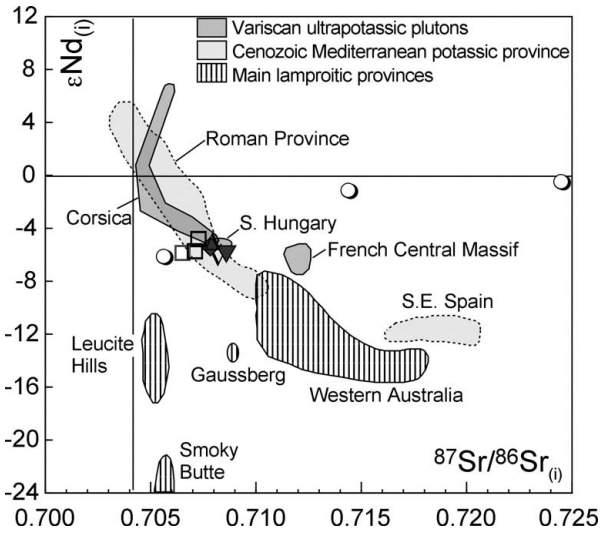

Figure 11. Initial εNd v. initial $^{87}Sr/^{86}Sr$. The $^{87}Sr/^{86}Sr$ of the 'Bulk Earth' has been calculated at 339 Ma (^{40}Ar–^{39}Ar dating on biotite, present work), using a present-day Sr isotope composition of 0.7045 and Rb/Sr = 0.029 (DePaolo & Wasserburg, 1976). For comparison are reported the fields of Variscan ultrapotassic plutons from southern Hungary (Buda & Dobosi, 2004), the French Central Massif (Livradois area: Solgadi *et al.* 2007) and Corsica (Cocherie *et al.* 1994), the Cenozoic Mediterranean potassic province and the main lamproite provinces (Wilson, 1991). For legend see Figure 4.

As a whole, these results are consistent with those obtained for coeval high-K plutons and their mafic enclaves from southern Hungary and the southern Bohemian Massif (Buda & Dobosi, 2004 and Gerdes, Wöerner & Finger, 2000 in Table 7) and, to a minor extent, the U_1 plutonic association from Corsica, occupying the 'orogenic mantle array' (Bonin, 2004). A compositional overlap between Svidnya lamproites and the Italian Roman Province field (Nelson, McCulloch & Sun, 1986; Fraser *et al.* 1985) is highlighted in Figure 11.

10. Igneous evolution

The geochemical data suggest the origin of Kfs–Cpx–Plg–Bt–Hbl-bearing monzodiorite inclusions and lamproites by fractionation from a common parental magma. In particular, major, trace and rare earth element contents of lamproites are in accordance with SiO_2-rich lamproitic compositions (Carlier & Lorand, 2003; Mitchell & Edgar, 2002), but the monzodiorite has a higher total ΣREE content.

Conversely, unequivocal cogenetic correlations between lamproites and syenites based on major and trace element chemistry are lacking. The rare occurrence of phlogopitized biotite in lamproites (Table 3) and metastable titanian phlogopite in syenites may suggest hybridization processes (Prelevic *et al.* 2004). However, the mineralogy, the whole rock compositions and the crystallization order in syenites suggest a melt richer in Na_2O, SiO_2 and H_2O. Different accessory minerals have also precipitated out; for example, Ba- and Nb-titanosilicates are lacking in lamproites, likely due to element partitioning in other silicates in spite of high contents in the bulk composition. For this reason, the mineral chemistry and microtextures are reliable evidence for two distinct hybridizations. The positive correlation between MgO and P_2O_5 and the variable Zr, Nb, Ce and Th in lamproites and syenites could reflect the melting of a source containing residual apatite, but with a heterogeneous distribution of other accessory minerals, possibly a veined mantle producing variably hybridized melts (Venturelli *et al.* 1988).

Syenites and quartz syenites show apparent HREE fractionation, likely an effect of cumulus plus fractional crystallization that also explains their ΣREE. Both in lamproites and in syenites, the negative Eu anomaly is inferred as inherited from the source, as the precipitation of sodic plagioclase only starts from syenite compositions.

Two evolved syenites deviate from the general Sr–Nd isotopic trend towards more ^{87}Sr radiogenic values, attributed to selective contamination with circulating fluids of crustal origin. These samples are also characterized by almost chondritic Nd isotopic values, implying a mantle source enriched in incompatible elements and LREE. This could be interpreted as the effect of melting of an isotopically heterogeneous source, characterized by different domains, which underwent distinct evolutionary trends from a pristine depleted mantle, as revealed by the initial Nd isotopic ratio obtained from model-ages.

For Mediterranean Cenozoic Fo-rich olivine-, Cr-rich spinel-bearing lamproites, olivine phenocrysts and xenocrysts are assumed as a proxy of a depleted component in the mantle source. In this case, an origin in an ultra-depleted lithospheric mantle affected by supra-subduction magmatism (boninites), followed by subduction of crustal-derived metasediments during the Alpine collision, has been suggested (Prelevic & Foley, 2007).

In the Balkan orogen, an island-arc association with a 572 Ma boninite protolith, tholeiites and flysch deposits in the East Rhodope (central-eastern Bulgaria: Haydoutov *et al.* 2004) and in the Moldanubian zone were subducted during the Variscan collision. Based on the isotopic ratios ($\varepsilon Nd_{339Ma} = -4.87$ to -6.35), lamproites, melasyenites and syenites share a similarly enriched mantle source. In this regard, the timing of subduction of the ultra-depleted lithospheric mantle is later than in the model of Prelevic & Foley (2007), however, the mechanism and the lithospheric components might be still comparable in the petrogenesis of Svidnya lamproites.

11. Geodynamic implications

The post-collisional high-K plutonism recorded in the Bohemian, Austro-Alpine, Vosges, French and Corsica

https://doi.org/10.1017/S0016756809990550 Published online by Cambridge University Press

domains likely has a genetic link with the subduction setting in evidence along the Variscan collision front. In particular, the European Variscan ultrapotassic plutons are generally interpreted as having originated in a post-collisional setting (e.g. Finger *et al.* 1997; Bonin, 2004). However, in detail, different mechanisms are invoked to account for their emplacement, such as (1) strike-slip tectonics (central Alps; Schaltegger *et al.* 1991), (2) extensional tectonics and uplift of deep crust (southern Hungary; Buda & Dobosi, 2004), and (3) magma ascent along the uplift channels of the associated high-pressure rocks, due to heating of an enriched mantle by asthenosphere, in a slab break-off setting (Moldanubian domain; Finger *et al.* 2007).

In the Bulgarian sector, ultrapotassic magmatism is coeval with the main Variscan tectonic and metamorphic stage and follows the exhumation from at least 40 km depth, of a migmatite- and eclogite-bearing gneiss–amphibolite complex dated at 398 ± 5.2 Ma by ^{39}Ar–^{40}Ar on hornblende, which represents the high-pressure record in the Sredna Gora terrane (≈ 1.2 GPa; Gaggero *et al.* 2008). Thermal re-equilibration, following break-off of the subducting plate, would induce the partial melting of those domains within the lithospheric mantle metasomatized during the oceanic subduction and/or earlier events (Davies & von Blanckenburg, 1995).

The strong enrichments in K, Rb, Ba and Th of Svidnya lamproites, and particularly the high Rb/Sr and Rb/Ba values, support the contribution of subducted sediments to the magma composition (e.g. Rogers *et al.* 1987), whereas the low Nb/Zr values indicate that a component from the partial melting of subduction-modified mantle cannot be excluded (Thompson & Fowler, 1986). The Nd model ages may date a Mesoproterozoic metasomatic event (1.3–1.5 Ga) and overlap with the 1.4–1.7 Ga indicated for the lithospheric mantle roots of the European Variscan fold belt (Liew & Hofmann, 1988).

During Carboniferous times, deformation propagated eastwards with the progressive closure of the Palaeotethys ocean. During this process, the western parts of the Variscan orogen were characterized by Himalayan-type continent–continent collision, whereas an Andean type ocean–continent setting is inferred in its eastern parts (Bonin, 2004). The roll-back of the subducting Palaeotethys slab has been invoked to account for the post-collisional ultrapotassic igneous products, such as in the External Crystalline Massifs of the Alps (von Raumer, Stampfli & Bussy, 2003). The model encompasses a stepwise development through: (1) lithosphere stacking and rapid uplift of the overriding plate, (2) decompression melting of an ultra-depleted mantle metasomatically enriched to originate ultrapotassic melts (Cocherie *et al.* 1994), (3) break-off of the subducted slab and partial melting in the overriding lithosphere at shallower depth, with production of alkaline and calc-alkaline melts (Finger *et al.* 2007; Holub, Cocherie & Rossi, 1997; (4) lithospheric thinning through delamination.

12. Conclusions

(1) The Svidnya suite reflects a polyphase crystallization history. The high-pressure record in lamproite is represented by olivine replaced by amphibole and by the anhydrous assemblage K-feldspar + diopsidic augite. The silica-undersaturated melt evolves towards silica and fluid saturation represented by the precipitation of high-Ti biotite and by the replacement/overgrowth of pyroxene by richterite, winchite and actinolite. In parallel, biotite crystallization suggests decompression during magma cooling. Following a two-phase hybridization process, the syenite magma evolved by fractional crystallization towards lower pressure conditions.

(2) The isotope and trace element geochemistry of the lamproites suggest an origin in the partial melting of a metasomatically enriched lithospheric mantle, ultra-depleted since the extraction of the Cambro-Ordovician boninites (Carrigan *et al.* 2006; Haydoutov *et al.* 2004). In the following eo-Variscan episode, crust subduction could provide the fertilization of the refractory depleted mantle.

(3) The remarkable variability between lamproites and syenite could be related to different extents of mantle metasomatism and subsequent partial melting. In particular, the partial melting of a veined mantle is liable to produce variably hybridized, though broadly similar, potassic melts (Foley, 1992). High-K calc-alkaline to shoshonitic to ultrapotassic magmas are thus also consistent with the monzodiorite inclusion in the lamproite.

(4) The Early Carboniferous (Visean) intrusion ages of 337 ± 4 Ma and 339.1 ± 1.6 Ma obtained by ^{39}Ar–^{40}Ar dating on the amphibole and biotite of Svidnya lamproites, respectively, provide evidence that the emplacement of lamproites followed the Variscan collision, pre-dating the conspicuous granite intrusions of Late Carboniferous age (311.9 ± 4.1 and 304.6 ± 4.0 Ma; Carrigan *et al.* 2005).

Acknowledgements. We acknowledge Laura Negretti for assistance with the microprobe analyses. We also thank Dejan Prelevic, Jürgen von Raumer, Anton Chakhmouradian and the editor David Pyle for very constructive suggestions. This research was carried out within the bilateral CNR (Italy) – BAN (Bulgaria) project headed by the late Luciano Cortesogno (Genoa University). Supplementary material for this paper is available in the online Appendix at http://journals.cambridge.org/geo.

References

BERGMAN, S. C. 1987. Lamproites and other potassium-rich igneous rocks: a review of their occurrence, mineralogy and geochemistry. In *Alkaline igneous rocks* (eds J. G. Fitton & B. G. J. Upton), pp. 103–89. Geological Society of London, Special Publication no. 30.

BONIN, B. 2004. Do coeval mafic and felsic magmas in post-collisional to within-plate regimes necessarily imply two contrasting, mantle and crustal, sources? A review. *Lithos* **78**, 1–24.

https://doi.org/10.1017/S0016756809990550 Published online by Cambridge University Press

BUDA, G. & DOBOSI, G. 2004. Lamprophyre-derived high-K mafic enclaves in Variscan granitoids from the Mecsek Mts. (South Hungary). *Neues Jahrbuch für Mineralogie, Abhandlungen* **180**(2), 115–47.

CARLIER, G. & LORAND, J. P. 2003. Petrogenesis of a zirconolite-bearing Mediterranean-type lamproite from the Peruvian Altipiano (Andean Cordillera). *Lithos* **69**, 15–35.

CARRIGAN, C. W., MUKASA, S. B., HAYDOUTOV, I. & KOLCHEVA, K. 2005. Age of Variscan magmatism from the Balkan sector of the orogen, central Bulgaria. *Lithos* **82**, 125–47.

CARRIGAN, C. W., MUKASA, S. B., HAYDOUTOV, I. & KOLCHEVA, K. 2006. Neoproterozoic magmatism and high-grade metamorphism in the Sredna Gora Zone, Bulgaria: An extension of the Gondwana-derived Avalonian–Cadomian belt? *Precambrian Research* **147**, 404–16.

COCHERIE, A., GUERROT, C. & ROSSI, P. 1992. Single-zircon dating by step-wise Pb-evaporation: Comparison with other geochronological techniques applied to the Hercynian granites of Corsica, France. *Chemical Geology* **101**, 131–41.

COCHERIE, A., ROSSI, P., FOUILLAC, A. M. & VIDAL, P. 1994. Crust and mantle contributions to granite genesis – An example from the Variscan batholith of Corsica, France, studied by trace element and Nd–Sr–O-isotope systematics. *Chemical Geology* **115**, 173–211.

CONTICELLI, S. 1998. The effect of crustal contamination on ultrapotassic magmas with lamproitic affinity: mineralogical, geochemical and isotope data from the Torre Alfina lavas and xenoliths, Central Italy. *Chemical Geology* **149**, 51–81.

CONTICELLI, S., D'ANTONIO, M., PINARELLI, L. & CIVETTA, L. 2002. Source contamination and mantle heterogeneity in the genesis of Italian potassic and ultrapotassic volcanic rocks: Sr–Nd–Pb isotope data from Roman Province and Southern Tuscany. *Mineralogy and Petrology* **74**(2–4), 189–222.

CORTESOGNO, L., GAGGERO, L., RONCHI, A. & YANEV, S. 2004. Late orogenic magmatism and sedimentation within Late Carboniferous to Early Permian basins in the Balkan terrane (Bulgaria): geodynamic implications. *International Journal of Earth Sciences* **93**, 500–20.

DAVIES, J. H. & von BLANCKENBURG, F. 1995. Slab breakoff: a model of lithosphere detachment and deformation in collisional orogens. *Earth and Planetary Science Letters* **129**, 85–102.

DEBON, F., GUERROT, C., MÉNOT, R.-P., VIVIER, G. & COCHERIE, A. 1998. Late Variscan granites of the Belledonne massif (French Western Alps): an Early Visean magnesian plutonism. *Schweizerische Mineralogische und Petrographische Mitteilungen* **78**, 67–85.

DEPAOLO, D. J. & WASSERBURG, G. J. 1976. Nd isotopic variations and petrogenetic models. *Geophysical Research Letters* **3**, 743–6.

DYULGEROV, M. M. & PLATEVOET, B. 2006. Unusual Ti and Zr aegirine–augite and potassic magnesio-arfvedsonite in the peralkaline potassic oversaturated Buhovo-Seslavtzi complex, Bulgaria. *European Journal of Mineralogy* **18**, 127–38.

FINGER, F., ROBERTS, M. P., HAUNSCHMID, B., SCHERMAIER, A. & STEYRER, H. P. 1997. Variscan granitoids of central Europe: their typology, potential sources and tectonothermal relations. *Mineralogy and Petrology* **61**, 67–96.

FINGER, F., GERDES, A., JANOUSEK, V., RENÉ, M. & RIEGLER, G. 2007. Resolving the Variscan evolution of the Moldanubian sector of the Bohemian Massif: the significance of the Bavarian and the Moravo-Moldanubian tectonometamorphic phases. *Journal of Geosciences* **52**, 9–28.

FOLEY, S. F. 1992. Vein-plus-wall-rock melting mechanisms in the lithosphere and the origin of potassic magmas. *Lithos* **28**, 435–53.

FOLEY, S. F., VENTURELLI, G., GREEN, D. H. & TOSCANI, L. 1987. The ultrapotassic rocks: characteristics, classification and constraints for petrogenetic models. *Earth Science Reviews* **24**, 81–134.

FRASER, K. J., HAWKESWORTH, C. J., ERLANK, A. J., MITCHELL, R. H. & SCOTT-SMITH, B. H. 1985. Sr, Nd and Pb isotope and minor element geochemistry of lamproites and kimberlites. *Earth and Planetary Science Letters* **76**, 57–70.

FUHRMAN, M. L. & LINDSLEY, D. H. 1988. Ternary-feldspar modeling and thermometry. *American Mineralogist* **73**, 201–15.

GAGGERO, L., BUZZI, L., HAYDOUTOV, I. & CORTESOGNO, L. 2008. Eclogite relics in the Variscan orogenic belt of Bulgaria (SE Europe). *International Journal of Earth Sciences,* doi: 10.1007/s00531-008-0352-x.

GERDES, A., WÖERNER, G. & FINGER, F. 2000. Hybrids, magma mixing and enriched mantle melts in post-collisional Variscan granitoids: the Rastenberg Pluton, Austria. In *Orogenic processes: Quantification and Modelling in the Variscan Belt* (eds W. Franke, V. Haak, O. Oncken & D. Tanner), pp. 415–31. Geological Society of London, Special Publication no. 179.

GROZDANOV, L. 1965. Uber die entstehungsfolge und die kristallisation der kalireiken alkaligesteine von Svidnja. *Bulletin de l'Institut Scientifique de Recherches Geologiques* **2**, 397–8.

GUTIÉRREZ-MARCO, J. C., YANEV, S., SACHANCKI, V., RÁBANO, I. & LAKOVA, I. 2003. New finding of trilobites and graptolites in the Ordovician in Bulgaria. *Review of the Bulgarian Geological Society* **63**(1–3), 51–8.

HAWTHORNE, F. C. & OBERTI, R. 2007. Classification of the amphiboles. *Reviews in Mineralogy & Geochemistry, Mineralogical Society of America, Geochemical Society, Accademia Nazionale dei Lincei* **67**, 55–88.

HAYDOUTOV, I. 1989. Precambrian ophiolites, Cambrian island arc, and Variscan suture in the South Carpathian–Balkan region. *Geology* **17**, 905–8.

HAYDOUTOV, I., KOLCHEVA, K., DAIEVA, L. A., SAVOV, I. & CARRIGAN, C. W. 2004. Island arc origin of the variegated formations from the East Rhodope, Bulgaria – Implications for the evolution of the Rhodope Massif. *Ofioliti* **29**, 145–57.

HAYDOUTOV, I. & YANEV, S. 1997. The Protomoesian microcontinent of the Balkan Peninsula – a peri-Gondwanaland piece. *Tectonophysics* **272**, 303–13.

HOLLAND, T. & BLUNDY, J. 1994. Non-ideal interactions in calcic amphiboles and their bearing on amphibole–plagioclase thermometry. *Contributions to Mineralogy and Petrology* **116**, 433–47.

HOLUB, F. V., COCHERIE, A. & ROSSI, P. 1997. Radiometric dating of granitic rocks from the Central Bohemian Plutonic Complex (Czech Republic): constraints on the chronology of thermal and tectonic events along the Moldanubian–Barrandian boundary. *Comptes Rendus Académie Sciences Paris* **325**, 19–26.

HUEBNER, J. S. & SATO, M. 1970. The oxygen fugacity-temperature relationships of manganese oxide and nickel oxide buffers. *American Mineralogist* **55**, 934–52.

JANOUSEK, V. & HOLUB, F. V. 2007. The causal link between HP–HT metamorphism and ultrapotassic magmatism in

collisional orogens: case study from the Moldanubian Zone of the Bohemian Massif. *Proceedings of the Geologists' Association* **118**, 75–86.

KLÖTZLI, U. S., BUDA, G. & SKIÖLD, T. 2004. Zircon typology, geochronology and whole rock Sr–Nd isotope systematics of the Mecsek Mountain granitoids in the Tisia Terrane (Hungary). *Mineralogy and Petrology* **81**, 113–34.

KRETZ, R. 1983. Symbols for rock-forming minerals. *American Mineralogist* **68**, 277–9.

LANGER, C., HEGNER, E., ALTHERR, R., SATIR, M. & HENJES-KUNST, F. 1995. Carboniferous granitoids from the Odenwald, the Schwarzwald and the Vosges: constraints on magma sources. *Terra Nostra* **95**, 114.

LEAKE, B. E., WOOLLEY, A. R., ARPS, C. E. S., BIRCH, W. D., GILBERT, M. C., GRICE, J. D., HAWTHORNE, F. C., KATO, A., KISCH, H. J., KRIVOVICHEV, V. G., LINTHOUT, K., LAIRD, J., MANDARINO, J. A., MARESCH, W. V., NICKEL, E. H., ROCK, N. M. S., SCHUMACHER, J. C., SMITH, D. C., STEPHENSON, N. C. N., UNGARETTI, L., WHITTAKER, E. J. W. & YOUZHI, G. 1997. Nomenclature of amphiboles: report of the subcommittee on amphiboles of the International Mineralogical Association, Commission on new minerals and mineral names. *Canadian Mineralogist* **35**, 219–46.

LEAKE, B. E., WOOLLEY, A. R., BIRCH, W. D., BURKE, E. A. J., FERRARIS, G., GRICE, J. D., HAWTHORNE, F. C., KISCH, H. J., KRIVOVICHEV, V. G., SCHUMACHER, J. C., STEPHENSON, N. C. N. & WHITTAKER, E. J. W. 2003. Nomenclature of amphiboles: additions and revisions to the International Mineralogical Association's 1997 recommendations. *Canadian Mineralogist* **41**, 1355–62.

LE BAS, M. J., LE MAITRE, R. W., STRECKEISEN, A. L. & ZANETTIN, B. 1986. A chemical classification of volcanic rocks based on the total alkali–silica diagram. *Journal of Petrology* **27**, 745–50.

LE BAS, M. J. & STRECKEISEN, A. L. 1991. The IUGS systematics of igneous rocks. *Journal of Geological Society, London* **148**, 825–33.

LIEW, T. C. & HOFMANN, A. W. 1988. Precambrian crustal components, plutonic associations, plate environment of the Hercynian Fold Belt of central Europe: indications from a Nd and Sr isotope study. *Contributions to Mineralogy and Petrology* **98**, 129–38.

LILOV, P., GROZDANOV, L. & PEEVA, I. 1968. On the absolute age for the magmatic rocks from the deposits of Svidnya and Seslavci. *Bulletin Geological Institute, Series Geochemistry, Mineralogy and Petrography* **17**, 79–82.

LUDWIG, K. R. 1994. *Analyst: a computer program for control of a thermal-ionization single-collector mass-spectrometer.* US Geological Survey Open File Report, 92–543.

MITCHELL, R. H. & BERGMAN, S. C. 1991. *Petrology of lamproites*. Plenum Press.

MITCHELL, R. H. & EDGAR, A. D. 2002. Melting experiments on SiO_2-rich lamproites to 6.4 GPa and their bearing on the sources of lamproite magmas. *Mineralogy and Petrology* **74**, 115–28.

MORIMOTO, N. 1988. Nomenclature of pyroxenes. *Schweizerische Mineralogische und Petrographische Mitteilungen* **68**, 95–111.

NASDALA, L., WENZEL, T., PIDGEON, R. T. & KRONZ, A. 1999. Internal structures and dating of complex zircons from Meissen Massif monzonites, Saxony. *Chemical Geology* **156**, 331–41.

NELSON, D. R., MCCULLOCH, M. T. & SUN, S. S. 1986. The origins of ultrapotassic rocks as inferred from Sr, Nd and Pb isotope. *Geochimica et Cosmochimica Acta* **50**, 231–45.

PAQUETTE, J.-L., MÉNOT, R.-P., PIN, C. & ORSINI, J.-B. 2003. Episodic and short-lived granitic pulses in a post-collisional setting: evidence from precise U–Pb zircon dating through a crustal cross-section in Corsica. *Chemical Geology* **198**, 1–20.

PRELEVIC, D. & FOLEY, S. F. 2007. Accretion of arc-oceanic lithospheric mantle in the Mediterranean: evidence from extremely high-Mg olivines and Cr-rich spinel inclusions in lamproites. *Earth and Planetary Science Letters* **256**, 120–35.

PRELEVIC, D., FOLEY, S. F., CVETKOVIC, V. & ROMER, R. L. 2004. Origin of Minette by Mixing of Lamproite and Dacite Magmas in Veliki Majdan, Serbia. *Journal of Petrology* **45**, 759–92.

PRELEVIC, D., FOLEY, S. F., ROMER, R. L. & CONTICELLI, S. 2008. Mediterranean Tertiary lamproites derived from multiple source components in postcollisional geodynamics. *Geochimica et Cosmochimica Acta* **72**, 2125–56.

ROCK, N. M. S. 1990. The International Mineralogical Association (IMA/CNMMN) Pyroxene nomenclature scheme: computerization and its consequences. *Mineralogy and Petrology* **43**, 99–119.

ROGERS, N. W., HAWKESWORTH, C. J., MATTEY, D. P. & HARMON, R. S. 1987. Sediment subduction and the source of potassium in orogenic leucitites. *Geology* **15**, 451–3.

RUDNICK, R. L. & GAO, S. 2004. Composition of the Continental Crust. In *Treatise on Geochemistry: volume 3 – The Crust* (eds H. D. Holland & K. K. Turekian), pp. 1–64. Amsterdam: Elsevier.

RUTHERFORD, M. J. 1973. The phase relations of aluminous iron biotite in the system $KAlSi_3O_8$–$KalSiO_4$–Al_2O_3–Fe–O–H. *Journal of Petrology* **14**, 159–80.

SABATIER, H. 1980. Vaugnérites et granites: une association particulière de roches grenues acides et basiques. *Bulletin de Minéralogie* **103**, 507–22.

SAVOV, I., RYAN, J., HAYDOUTOV, I. & SCHIJF, J. 2001. Late Precambrian Balkan–Carpathian ophiolite – a slice of the Pan-African ocean crust? Geochemical and tectonic insights from the Tcherni Vrah and Deli Jovan massifs. Bulgaria and Serbia. *Journal of Volcanological Geothermal Research* **110**, 299–318.

SCHALTEGGER, U., GNOS, E., KÜPFER, T. & LABHART, T. P. 1991. Geochemistry and tectonic significance of Late Hercynian potassic and ultrapotassic magmatism in the Aar Massif (Central Alps). *Schweizerische Mineralogische und Petrographische Mitteilungen* **71**, 391–403.

SCHALTEGGER, U., SCHNEIDER, J.-L., MAURIN, J.-C. & CORFU, F. 1996. Precise U–Pb chronometry of 345–340 Ma old magmatism related to syn-convergence extension in the Southern Vosges (Central Variscan Belt). *Earth and Planetary Science Letters* **144**, 403–19.

SOLGADI, F., MOYEN, J.-F., VANDERHAEGHE, O., SAWYER, E. W. & REISBERG, L. 2007. The role of crustal anatexis and mantle-derived magmas in the genesis of synorogenic Hercynian granites of the Livradois area, French Massif Central. *Canadian Mineralogist* **45**, 581–606.

SPEAR, F. S. & CHENEY, J. T. 1989. A petrogenetic grid for pelitic schists in the system K_2O–FeO–MgO–Al_2O_3–SiO_2–H_2O. *Contributions to Mineralogy and Petrology* **101**, 149–64.

https://doi.org/10.1017/S0016756809990550 Published online by Cambridge University Press

STEFANOVA, M. 1966. Petrochemical peculiarities of the Svidnya potassium alkaline rocks. *Bulletin of 'Strasimir Dimitrov' Institute of Geology* Kh. XV, 191–203.

STEFANOVA, M., PAVLOVA, M. & AMOV, B. 1974. Geochemistry and isotopic composition of lead from potassium-alkaline rocks of lamproite character. In *Mineral Genesis*, pp. 333–48. Sofia: Bulgarian Academy of Science (in Bulgarian).

SUN, S. S. & MCDONOUGH, W. F. 1989. Chemical and isotopic systematics of oceanic basalts: implications for mantle composition and processes. In *Magmatism in ocean basins* (eds A. D. Saunders & M. J. Norry), pp. 313–45. Geological Society of London, Special Publication no. 42.

THOMPSON, R. N. & FOWLER, M. B. 1986. Subduction-related shoshonitic and ultrapotassic magmatism: a study of Siluro-Ordovician syenites from the Scottish Caledonides. *Contributions to Mineralogy and Petrology* **94**, 507–22.

VENTURELLI, G., MARIANI, E. S., FOLEY, S. F., CAPEDRI, S. & CRAWFORD, A. J. 1988. Petrogenesis and conditions of crystallization of Spanish lamproitic rocks. *Canadian Mineralogist* **26**, 67–79.

VILLA, I. M., GROBÉTY, B., KELLEY, S. P., TRIGILA, R. & WIELER, R. 1996. Assessing Ar transport paths and mechanism in the McClure Mountains hornblende. *Contributions to Mineralogy and Petrology* **126**, 67–80.

VLADYKIN, N. V., GROZDANOV, L. A. & BONEV, I. K. 2001. Chemical composition and geochemical characteristics of the Svidnya magmatic potassic-alkaline association, Western Stara Planina Mountain. *Geochemistry, Mineralogy and Petrology* **38**, 3–22.

VON RAUMER, J. F., BUSSY, F. & STAMPFLI, G. M. 2009. The Variscan evolution in the External massifs of the Alps and place in their Variscan framework. *Comptes Rendus Geoscience* **341**(2–3), 239–52.

VON RAUMER, J. F., STAMPFLI, G. M. & BUSSY, F. 2003. Gondwana-derived microcontinents – the constituents of the Variscan and Alpine collisional orogens. *Tectonophysics* **365**, 7–22.

WARTHO, J.-A. 1995. Apparent argon diffusive loss $^{40}Ar/^{39}Ar$ age spectra in amphibole. *Earth and Planetary Science Letters* **134**, 393–407.

WEN, S. & NEKVASIL, H. 1994. SOLVCALC: an interactive graphics program package for calculating the ternary feldspar solvus and for two-feldspar geothermometry. *Computers & Geosciences* **20**, 1025–40.

WENZEL, T., MERTZ, D. F., OBERHÄNSLI, R., BECKER, T. & RENNE, P. R. 1997. Age, geodynamic setting, and mantle enrichment processes of a K-rich intrusion from the Meissen Massif (Northern Bohemian Massif) and implications for related occurrences from Mid-European Hercynian. *Geologische Rundschau* **86**, 556–70.

WILSON, M. 1991. *Igneous petrogenesis: a global tectonic approach*. Harper Collins.

WONES, D. R. 1972. Stability of biotite: A reply. *American Mineralogist* **57**, 316–17.

WONES, D. R. & EUGSTER, H. P. 1965. Stability of biotite: experiment theory and application. *American Mineralogist* **50**, 1228–72.

WOOLLEY, A. R., BERGMAN, S. C., EDGAR, A. D., LE BAS, M. J., MITCHELL, R. H., ROCK, N. M. S. & SCOTT SMITH, B. H. 1996. Classification of lamprophyres, lamproites, kimberlites and the kalsilitic, melilitic, and leucitic rocks. *Canadian Mineralogist* **34**, 175–86.

YANEV, S. 2000. Palaeozoic terranes of the Balkan Peninsula in the framework of Pangaea assembly. *Palaeogeography, Palaeoclimatology, Palaeoecology* **161**, 151–77.

https://doi.org/10.1017/S0016756809990550 Published online by Cambridge University Press